Article:
Garrett, Ed, Melnick, Daniel, Dura, Tina et al. (5 more authors) (2020) Holocene relative sea-level change along the tectonically active Chilean coast. Quaternary Science Reviews. 106281. ISSN 0277-3791

https://doi.org/10.1016/j.quascirev.2020.106281

Holocene relative sea-level change along the tectonically active Chilean coast

Ed Garrett[1]*, Daniel Melnick[2], Tina Dura[3], Marco Cisternas[4], Lisa L. Ely[5], Robert L. Wesson[6], Julius Jara-Muñoz[7] and Pippa L. Whitehouse[8]

[1] Department of Environment and Geography, University of York, York, UK

[2] Instituto de Ciencias de la Tierra, TAQUACh, Universidad Austral de Chile, Valdivia, Chile

[3] Department of Geosciences, Virginia Tech, Blacksburg, VA, USA

[4] Instituto de Geografía, Pontificia Universidad Católica de Valparaíso, Valparaíso, Chile

[5] Department of Geological Sciences, Central Washington University, Ellensburg, WA, USA

[6] U.S. Geological Survey, Denver, CO, USA

[7] Department of Earth and Environmental Sciences, University of Potsdam, Potsdam, Germany

[8] Department of Geography, Durham University, Durham, UK

*Corresponding author: ed.garrett@york.ac.uk, Wentworth Way, Heslington, York, YO10 5NG, United Kingdom

Abstract

We present a comprehensive relative sea-level (RSL) database for north, central, and south-central Chile (18.5°S – 43.6°S) using a consistent, systematic, and internationally comparable approach. Despite its latitudinal extent, this coastline has received little rigorous or systematic attention and details of its RSL history remain largely unexplored. To address this knowledge gap, we re-evaluate the geological context and age of previously published sea-level indicators, providing 78 index points and 84 marine or terrestrial limiting points spanning from 11 ka to the present day. Many data points were originally collected for research in other fields and have not previously been examined for the information they provide on sea-level change. Additionally, we describe new sea-level data from four sites located between the Gulf of Arauco and Valdivia. By compiling RSL histories for 11 different regions, we summarise current knowledge of Chilean RSL. These histories indicate mid Holocene sea levels above present in all regions, but at highly contrasting elevations from ~30 m to < 5 m. We compare the spatiotemporal distribution of sea-level data points with a suite of glacial isostatic adjustment models and place first-order constraints on the influence of tectonic processes over 10^3 to 10^4 year timescales. While seven regions indicate uplift rates < 1 m ka^{-1}, the remaining regions may experience substantially higher rates. In addition to enabling discussion of the factors driving sea-level change, our compilation provides a resource to assist attempts to understand the distribution of archaeological, palaeoclimatic, and palaeoseismic evidence in the coastal zone and highlights directions for future sea-level research in Chile.

Keywords: Holocene; Sea-level changes; South America; Data analysis; Sea-level database; Glacial isostatic adjustment; Tectonics

1. Introduction

Eustatic, isostatic, tectonic, and local factors drive changes in Holocene relative sea level (RSL) (Farrell and Clark, 1976; Pirazzoli, 1991). Compilations of regional databases of Holocene index points, which constrain the age and elevation of past sea level, advance our understanding of the mechanisms and relative contributions of these driving factors in time and space. They highlight regional differences, provide constraints on glacial isostatic adjustment models and serve as a baseline for assessing future sea-level changes (Shennan et al., 2012, 2018; Engelhart et al., 2015; Khan et al., 2015; Vacchi et al., 2016). Despite extending through more than 37° of latitude, the Chilean coastline has not previously received rigorous or systematic attention, and details of its RSL history remain poorly understood. While previous coastal zone investigations have focussed on archaeology (e.g. Pino and Navarro, 2005; May et al., 2015), palaeoseismology (e.g. Cisternas et al., 2005; 2017; Dura et al., 2015; 2017; Garrett et al., 2015), tectonics (e.g. Stefer et al., 2010; Melnick et al., 2019), and palaeoclimate (e.g. Villa-Martínez and Villagrán, 1997; Frugone-Álvarez et al., 2017), only a limited number of studies have specifically addressed Holocene sea-level evolution (e.g. Leonard and Wehmiller, 1991; Atwater et al., 1992; Nelson and Manley, 1992). The limited scope of previous Holocene sea-level data compilations (Isla, 1989; Isla et al., 2012) and the potential to increase the temporal and spatial resolution of RSL histories in Chile using data from other fields of study necessitates a reappraisal of RSL data from this region.

For the first time, this paper compiles a comprehensive sea-level database for north, central, and south-central Chile (18.5°S – 43.6°S; Fig. 1) using a consistent, systematic, and internationally comparable approach (Hijma et al., 2015; Khan et al., 2019). Our database incorporates a range of different types of sea-level indicators, including tidal marsh sediments, beach ridges, marine deposits and freshwater sediments, dated using radiocarbon and luminescence approaches. We re-evaluate the geological context and age of previously published sea-level data, providing 78 index

points (reconstructions of the elevation of RSL at a specific time and location) and 84 limiting points (which place minimum or maximum constraints on the elevation of RSL) that span the period from 11000 years ago to the present day. We also present a new index point and three new limiting points from four sites between 35.8°S and 43.6°S. By compiling and comparing the RSL history for 11 different regions, we seek to summarise current knowledge of Chilean RSL, highlight directions for future sea-level research, and provide a resource to assist research into archaeological, palaeoclimatic, and palaeoseismic records in the coastal zone.

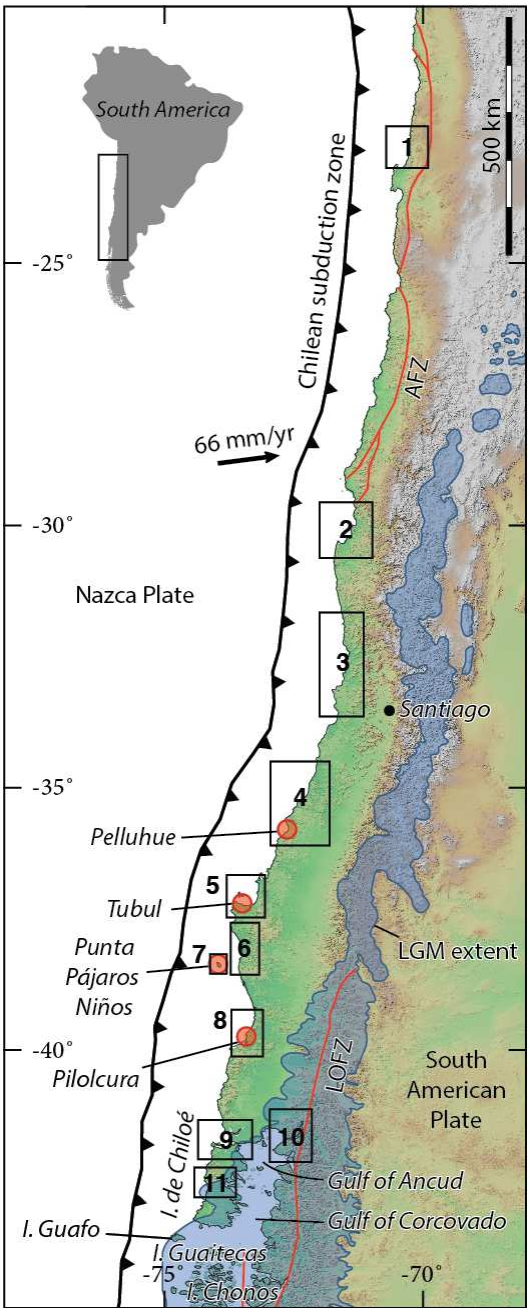

Figure 1: Location of the sea-level data points assessed in this study, grouped into regions (black boxes). Red circles indicate new sites reported here for the first time. AFZ: Atacama fault zone, LOFZ: Liquiñe-Ofqui fault zone, LGM: Last Glacial Maximum extent of the Patagonian ice sheet (blue shading, following Ehlers et al., 2011).

2. Study area

We restrict our review of published sea-level data to the coastline between Arica (18.5°S) and Isla Guafo (43.6°S), a straight-line distance of almost 3000 km (Fig. 1). This coastline possesses a consistent tectonic setting, characterised by subduction of the Nazca Plate beneath South America. Despite the continuity in tectonic setting between Isla Guafo and the triple junction, close to the Taitao Peninsula (46.5°S), we do not discuss sites in this region due to the complex tidal regimes associated with the fjord setting. Due to its remote nature, few published Holocene sea-level records currently exist between Isla Guafo and the Taitao Peninsula; however, we note that Reyes et al. (2018) discuss coastal archaeological sites from the Guaitecas (43.9°S) and Chonos (45.3°S) archipelagos and provide minimum ages for the marine terraces on which these sites are located. While increased tidal ranges also influence sites bordering the gulfs of Ancud and Corcovado on the western side of Isla de Chiloé (Fig. 1), we include the small number of data points available from this area due to their proximity to sites facing the open ocean. Sea-level data are available from the southernmost regions of Chile (e.g. Porter et al., 1984; Rabassa et al., 1986; Gordillo et al., 1992; McCulloch and Davies, 2001; Bentley and McCulloch, 2005); however, the unique glacial history of this region, the different tectonic setting, and the importance of local postglacial faulting mean they deserve a separate analysis and lie beyond the scope of this paper.

2.1 Tectonic setting

In contrast to the largely stable locations on which the majority of previous sea-level databases focus, Chilean RSL change is influenced by significant tectonic activity associated with the subduction of the Nazca Plate. Plate convergence induces both folding and faulting within the overriding South American Plate and deformation associated with megathrust earthquakes on the subduction interface (Barrientos, 2007). Since the start of the 20th century, at least eight Chilean earthquakes have exceeded magnitude (M_w) 8, including the largest event since the inception of modern seismic recording, the 1960 CE M_w 9.5 Valdivia earthquake and the 2010 CE M_w 8.8 Maule earthquake.

Decimetre- to metre-scale coseismic land-surface deformation accompanies these great earthquakes, resulting in abrupt relative sea-level changes over hundreds to thousands of kilometres of coastline (Plafker and Savage, 1970; Farías et al., 2010; Dura et al., 2017). Major interplate earthquakes (magnitude 7 – 8), occurring along the margin at a rate of ~50 per century, may also result in decimetre-scale land-surface deformation along tens of kilometres of coastline (Xu, 2017; Garrett et al., 2019). The sea-level history of tectonically active regions reflects these vertical coseismic changes and also the slower postseismic and interseismic deformation associated with strain accumulation between earthquakes.

In addition to deformation associated with slip on the subduction interface, concurrent splay faulting within the upper plate may contribute to abrupt local decimetre- to metre-scale changes in relative sea level (Melnick et al., 2012; Jara-Muñoz et al., 2017). Upper plate faults may also rupture quasi-independently of the megathrust. Two major fault systems lie parallel to the convergent margin (Fig. 1): the Atacama fault zone of the northern coastal cordillera and the Liquiñe-Ofqui fault zone, a dextral intra-arc transform fault of the main cordillera of south-central and southern Chile (Cembrano *et al*., 1996; Rosenau et al., 2006; Rehak *et al*., 2008). Instrumentally recorded earthquakes associated with these structures have not exceeded M_w 6.2 or produced evident coseismic coastal deformation (Barrientos, 2007; Lange et al., 2008).

2.2 Glacial history

At the maximum extent of the last glacial period, the Patagonian ice sheet extended along the Andes from ~38°S to ~56°S (Caldenius, 1932; Denton et al., 1999; Hulton et al., 2002; Glasser et al., 2008). The distribution of moraines and outwash plains suggests a piedmont lobe extended from the mainland and overran the southern half of Isla de Chiloé (Fig. 1), while northern Isla de Chiloé and the coastline of the mainland to the north remained ice free (Heusser and Flint, 1977; García, 2012).

In the south, the Patagonian ice sheet covered the Chilean mainland and outlying islands, with a modelled volume equivalent to 1.2 m of global sea level (Hulton et al., 2002). Patagonian piedmont glaciers rapidly retreated after 17500 – 17150 a BP (Denton et al., 1999; McCulloch et al., 2000), with the ice sheet losing over 80 % of its Last Glacial Maximum volume within 2000 years (Hulton et al., 2002). Relative warmth characterised the period from 13500 to 4000 a BP (Heusser and Streeter, 1980; Rabassa and Clapperton, 1990), before late Holocene cooling and increases in precipitation resulted in Neoglacial icefield expansion (Glasser at al., 2004; Bertrand et al., 2012). Three or four periods of glacier advance ensued, including during the Little Ice Age (Mercer, 1970; Aniya, 1996; Araneda et al., 2007). Subsequent retreat has reduced the combined contemporary extent of the North and South Patagonian icefields (47°S – 51°S) and the smaller, discontinuous icefields of the Cordillera Darwin (54°S – 55°S) to 17,000 km^2 (Rignot *et al*., 2003). The contribution of the two larger icefields to global sea-level rise has averaged 0.0052 ± 0.0008 mm yr^{-1} since 1870 (Glasser et al., 2011). This figure has increased to 0.067 ± 0.004 mm yr^{-1} between 2000 and 2012 (Willis et al., 2012).

3. Database methodology

Through a series of International Geological Correlation Programme and International Geoscience Programme (IGCP) projects (numbers 61, 200, 274, 367, 437, 495, 588 and 639), the sea-level community has derived and implemented standardised and globally applicable approaches to sea-level reconstruction. Integral to this endeavour, sea-level databases synthesise data from different studies to reconstruct regional relative sea-level histories (Bloom, 1977; Pirazzoli, 1991; Shennan et al., 2002; Khan et al., 2019). Databases contain sea-level index points, reconstructions of the elevation of RSL at a specific time and location, and limiting points, which place minimum or maximum constraints on the elevation of RSL (marine and terrestrial limiting points respectively). Our database compiles sea-level indicators from the literature, interpreting data from a wide range

of sources as either index or limiting points. For each data point, we quantify sources of vertical and temporal uncertainty following the approach set out by Hijma et al. (2015).

We subdivide our database into 11 regions based primarily on the proximity and clustering of sites. We assign sites to regions minimising the distances between sites within a region and maximising the distances between regions. The mean distance between a site and the centroid of its respective region is 22 km, with the centroids of adjacent regions generally separated by > 100 km. Despite the shorter distance between sites on Isla Mocha (region 7) and the adjacent mainland (region 6), we separate these regions based on their different tectonic histories (Nelson and Manley, 1992). Further subdivision to a finer spatial scale is currently unwarranted due to the low total number of sites and data points.

3.1 Data sources

Few studies have explicitly focussed on the history of RSL change in Chile; consequently, our data are principally derived from coastal investigations with different foci. In central and south-central Chile, we reanalyse sea-level indicators resulting from investigations into the occurrence of Holocene subduction zone earthquakes and tsunamis (e.g. Atwater et al., 1992; Cisternas et al., 2005; Nelson et al., 2009; Ely et al., 2014; Dura et al., 2015; Garrett et al., 2015; Hong et al., 2017). We also obtain sea-level data from datasets previously used to constrain tectonic uplift rates (Stefer et al., 2010; Melnick et al., 2019), identify human occupation of the coastal zone (Pino and Navarro, 2005), and reconstruct palaeoclimatic change (Villa-Martínez and Villagrán, 1997; Frugone-Álvarez et al., 2017). In northern and north-central Chile, we incorporate sea-level data from studies that have sought to constrain the age and elevation of mid-Holocene RSL (e.g. Ota and Paskoff, 1993; May et al., 2013; Hart et al., 2017). Similar RSL-focussed investigations in central and south-central Chile are less numerous (e.g. Nelson and Manley, 1992; Isla et al., 2012). Previous compilations included just three

(Isla, 1989) and ~30 (Isla et al., 2012) sea-level data points from our regions of interest. The use of a wider range of data sources provides a substantially expanded compilation and, for the first time, our compilation incorporates comprehensive data quality control and error assessment.

3.2 Indicative meaning

To serve as an index point, a sea-level indicator must have a defined relationship with tidal levels, or *indicative meaning* (van de Plassche, 1986; Shennan, 2015). The indicative meaning consists of the *reference water level*, the elevation at which the indicator occurs with respect to contemporaneous tidal levels, and the *indicative range*, the span of elevations at which the indicator might be found. We define indicative ranges for seven different types of index points and define reference water levels as the mid-points of the indicative ranges (Table 1). We obtain tidal datums for each location, modelling mean lower low water (MLLW), mean low water (MLW), mean tide level (MTL), mean high water (MHW), mean higher high water (MHHW), and highest astronomical tide (HAT) using the TPXO8-ATLAS global model of ocean tides (Egbert and Erofeeva, 2010). We scale the modelled tidal amplitude for each location following analysis of the differences between the tidal model and data from 21 permanent tide gauge stations (supplementary information S1).

Table 1: Definition of the indicative meaning of the different sea-level indicators assessed in this study. The reference water level is defined as the midpoint of the indicative range. HAT: Highest Astronomical Tide, MHHW: Mean Higher High Water; MHW: Mean High Water, MTL: Mean Tide Level, MLLW: Mean Lower Low Water.

Sample type	Evidence	Reference water level	Indicative range
Index points			
High tidal marsh environment	Organic sediments. High marsh plant macrofossils. Diatom or foraminiferal assemblages dominated by high marsh taxa.	(MHW+HAT)/2	MHW – HAT
Low tidal marsh/upper tidal flat environment	Organic or clastic sediments. Low marsh plant macrofossils. Diatom or foraminiferal assemblages dominated by low marsh/upper tidal flat taxa.	(MTL+MHW)/2	MTL – MHW

Undifferentiated tidal marsh environment	Organic sediments. Microfossil and macrofossil assemblages dominated by tidal marsh taxa that do not meet the requirements to be classified as strictly low or high tidal marsh.	(MTL+HAT)/2	MTL – HAT
Specified tidal marsh environment	Estimate of RWL and IR from quantitative approach e.g. microfossil transfer function.	Uniquely defined	Uniquely defined
Undifferentiated intertidal environment	Clastic sediments. Microfossils a mix of marine, brackish and freshwater species. May be supported by geomorphic setting.	(MLLW+HAT)/2	MLLW – HAT
Beach ridges	Sand- or gravel-rich shore-parallel ridges with a gently dipping or horizontal landward surface and a more steeply dipping seaward face.	HAT+1.5 m	HAT – HAT+3m
Undifferentiated beach environment	Sand- or gravel-rich sediments, may contain shells or shell fragments. Includes beachface, berm and beach ridge environments.	(MLLW – HAT+3m)/2	MLLW – HAT+3m
Limiting points			
Marine sediments	Clastic sediments containing marine diatom or foraminiferal assemblages or in-situ marine shells.	MTL	Below MTL
	Clastic sediments without (or without reported) identifiable macrofossils or microfossils.	MHHW	Below MHHW
	Coquina containing transported intertidal or subtidal molluscs but lacking morphology indicative of supratidal beach ridge deposition.	HAT	Below HAT
	Undifferentiated clastic sediments where neither beach ridge nor subtidal deposition can be discounted	HAT+3m	Below HAT+3m
Terrestrial sediments	Organic soil or peat with freshwater microfossil assemblages or in-situ freshwater plant macrofossils (e.g. tree stumps).	HAT	Above HAT
	Organic soil or peat without (or without reported) identifiable intertidal macrofossils or microfossils.	MTL	Above MTL
	Organic or clastic sediments with sedimentary structures, faunal or floral assemblages, or geochemical composition typical of lacustrine sedimentation.	HAT	Above HAT
	Clastic sediments exhibiting sedimentary structures typical of aeolian dunes.	HAT	Above HAT
	Clastic sediments exhibiting sedimentary structures typical of colluvial wedges.	HAT	Above HAT

208

209 Tidal marsh environments provide the majority of our index points. We separate these into low
210 marsh, high marsh, undifferentiated marsh, and specified marsh environments based on macro- and
211 microfossil evidence (Atwater et al., 1992; Nelson et al., 2009; Garrett et al., 2015). Specified tidal
212 marsh refers to samples with indicative meanings provided in the original study by the statistical
213 comparison of modern and fossil microfossil assemblages, usually diatoms, using transfer functions
214 (e.g. Garrett et al., 2015). The second largest group of index points come from beach ridges and
215 undifferentiated beach environments. The relationship between the elevation of a beach ridge crest

and coeval sea level is complex, with elevation reflecting wave run-up and other sediment transport mechanisms (Orford et al., 1991; Otvos, 2000; Tamura, 2012). Tamura (2012) recommends that sandy beach ridges are not used as sea-level indicators as the uncertainties involved are frequently too large in comparison with reconstructed sea-level changes since the mid Holocene. As we are not seeking to identify small-scale sea-level changes, we choose to incorporate sandy beach ridges and account for uncertainties using appropriately cautious indicative ranges. Furthermore, the presence of low elevation modern ridges and the occurrence of multiple fossil ridges at low elevations indicates Chilean beach ridges form within a few metres of contemporaneous sea level (Nelson and Manley, 1992; Bookhagen et al., 2006). On the Atlantic coast of Patagonia, Schellmann and Radtke (2010) suggest that beach ridge crests lie between 2 and 3 m above the highest tide level on exposed shorelines and down to 1 m or less above the highest tides in wave-protected areas. In this work, we conservatively consider beach ridge crests to lie between HAT and 3 m above HAT (Table 1). Where sediments are described by the original authors as “beach deposits” or similar, we extend the indicative range described above for beach ridges to include the intertidal zone (i.e. between MLLW and HAT + 3m). A similar approach was recently used by Vacchi et al. (2018) in eastern Canada.

Terrestrial and marine limiting points each have a reference water level, but as their precise relationship with contemporaneous sea level is unknown, their indicative ranges are simply open-ended windows above or below the reference water level (Table 1). Marine limiting points include clastic sediments containing in situ marine macro- or microfossils, coquinas (deposits largely consisting of reworked shells), and clastic sediments without (or without reported) fossils. Terrestrial limiting points include freshwater marshes, lake sediments, and aeolian dunes. We use above MTL as a conservative indicative range, unless unequivocal evidence (e.g. in situ tree roots) warrants the use of HAT as the reference water level (Table 1).

3.3 Quantifying vertical uncertainties

242

243 We account for errors in the vertical position of each sea-level indicator, considering uncertainties in
244 the sample depth and the absolute elevation of the top of the core, pit or exposure. Where these
245 uncertainties are not explicitly stated by the original authors, we estimate appropriate values
246 following Hijma et al. (2015). Where elevations are related to "mean sea level" (including datums of
247 uncertain meaning such as "sea level", "modern sea level") or other tidal levels, and lack further
248 details of how they were derived, we define the corresponding tidal uncertainty as ± 0.5 m, in
249 keeping with the magnitude of uncertainties proposed by Hijma et al. (2015) for elevations derived
250 from vegetation zones, digital elevation models, or using water depth measurements. Where sample
251 elevations are relative to tidal levels measured using a portable tide gauge, with measurements over
252 hours or days, we estimate the corresponding uncertainty as ± 0.07 m following Wesson et al.
253 (2014). In the absence of local conversions from a reference geoid to mean sea level, where
254 elevations are given with respect to the EGM96 geoid, we do not account for differences between
255 this model and MSL. We do, however, include a vertical error of ± 0.20 m to reflect the uncertainty
256 of this conversion (or lack thereof), reflecting the magnitude of the offsets identified for the Gulf of
257 Arauco by González-Acuña (2012). We note that the future application of geoid undulation models
258 may change the elevation of a small number of index and limiting points.

259

260 To account for disparities between the tidal model—which does not incorporate atmospheric
261 effects—and actual tides, we include a further vertical uncertainty associated with modelling each
262 reference water level based on a comparison of model predictions and data from 21 permanent tide
263 gauges (supplementary information S1). This uncertainty is calculated as a percentage of the
264 modelled reference water level and is site and sample-type specific, ranging from <0.01 m to 0.27 m.

265

266 3.4 Accounting for tectonics, compaction and tidal range changes

267

For sites within the rupture zone of the 2010 Maule earthquake, where elevations were determined before 2010, we adjust for coseismic deformation using estimates of uplift or subsidence, with corresponding errors, from published field data (Farías et al., 2010; Melnick et al., 2012). Due to a lack of data, we do not adjust for postseismic deformation following the 2010 earthquake. Similarly, for sites outside the 2010 rupture area, we do not account for changes in RSL caused by interseismic deformation or other processes occurring between the timing of data collection and the present day. We do not correct for millennial-scale tectonic motions before presenting regional sea-level histories; rather, we choose to discuss reconstructed relative sea-level changes with respect to driving factors including tectonics.

The majority of Chilean index and limiting points come from intercalated rather than basal settings and may be influenced by compaction. Intense seismic shaking could potentially exacerbate this phenomenon. Sediment compaction after deposition lowers intercalated sedimentary sea-level indicators, but does not influence basal data points (Horton and Shennan, 2009; Brain et al., 2012). Noting a lack of work on compaction in South American marshes and the scarcity of information on the depth to consolidated strata for many sea-level indicators in the database, we do not attempt to apply a correction for this factor.

Due to the predominantly linear and open configuration of the Chilean coast, we anticipate that latitudinal variations in tidal range are likely to have been consistent over the Holocene. Sites fringing the semi-enclosed gulfs on the eastern side of Isla de Chiloé are more likely to have experienced changes in tidal range; however, with the small number of data points from this region and without further information available on palaeotidal ranges, we do not consider this process in the current compilation.

3.5 Chronological control

Radiocarbon and luminescence approaches provide ages for each of the sea-level indicators. Where publications use radiocarbon dating, we recalibrate all ages using OxCal v.4.2 (Bronk Ramsey, 2009) and the latest calibration curves: ShCal13 (Hogg et al., 2013), Marine13 (Reimer et al., 2013), and Bomb13: southern hemisphere zone (Hua et al., 2013). An offset from the global marine reservoir (ΔR) must be applied where radiocarbon dates relate to marine samples; however, the Chilean coastline is poorly represented in the global marine reservoir database (http://calib.org/marine/). Two samples from Valparaíso (33°S) provide contrasting offsets of 61 ± 50 years (Ingram and Southon, 1996) and 313 ± 76 years (Taylor and Berger, 1967). To reflect this uncertainty, we use the weighted average of these samples, 137 ± 164 years, as the offset for all locations south of 28.5°S. Towards the northern limit of the region discussed here, Taylor and Berger (1967) report an offset of 175 ± 34 years from Antofagasta (24°S). Ortlieb et al. (2011) report temporally variable ΔR values from between 14°S and 24°S. We employ their mid to late Holocene mean value of 226 ± 98 years as the offset for the single site included in our database that lies north of 28.5°S.

3.6 Data visualisation

On figures summarising the age and elevation of sea-level data points, we plot sea-level index points as rectangles, with the height proportional to the vertical uncertainty in RSL and the width proportional to the 2σ age range. Following Hijma et al. (2015), we plot terrestrial limiting dates as green T-shaped symbols and marine limiting dates as blue ⊥-shaped symbols. An arrowhead at the end of the vertical line points towards RSL lying below (for T-shaped terrestrial limiting points) or above (for ⊥-shaped marine limiting points) the horizontal line, which sits at the extreme limit of the uncertainty range. The length of the vertical line reflects the total vertical uncertainty. We note that some studies have inverted the use of these symbols (Vacchi et al., 2016; Khan et al., 2017; García-

319 Artola et al., 2018), although not the colours, and care must consequently be taken to ensure that
320 the intended meaning is fully understood.
321
322 3.7 Modelling glacial isostatic adjustment and tectonic uplift
323
324 To investigate the processes driving RSL change, we compare sea-level data with glacial isostatic
325 adjustment (GIA) models. A GIA model requires two inputs: information about past global ice sheet
326 change (the 'ice model') and information about the rheological properties of the solid Earth (the
327 'Earth model'). For the purposes of this study, we assume Earth structure varies only radially,
328 enabling us to define a series of 'one-dimensional' Earth models that differ in terms of the values
329 assumed for lithospheric thickness and upper/lower mantle viscosity. For each of the 11 regions, we
330 predict RSL at the centre of each region at 1 ka intervals using two ice models, ICE-5G (Peltier, 2004)
331 and ICE-6G (Peltier et al., 2015). Each ice model is combined with 12 one-dimensional Earth models
332 that encompass a realistic range of rheologies for the subduction zone. We use lithospheric
333 thicknesses of 71, 96 and 120 km and upper mantle viscosities of 5×10^{19} Pa s, 8×10^{19} Pa s, 1×10^{20}
334 Pa s, and 2×10^{20} Pa s, with a lower mantle viscosity of 10^{22} Pa s. Our upper mantle viscosities are
335 lower than those typically used in passive margin settings (e.g. Shennan et al., 2018; Vacchi et al.,
336 2016) and in previous studies of coastal palaeoseismic evidence (Dura et al., 2016). As such, they
337 more closely reflect rheologies inferred at seismic-cycle timescales in Chile (Khazaradze et al., 2002;
338 Lorenzo-Martin et al., 2006; Li et al., 2018) and other subduction zones (e.g. Wiseman et al., 2015;
339 Freed et al., 2017). Studies of crustal rebound following recent ice loss from the Patagonian Icefields
340 similarly suggest low upper mantle viscosities (Lange et al., 2014; Richter et al., 2016).
341
342 To assess the possible role and rates of millennial-scale tectonic uplift, we apply a range of linear
343 corrections to the RSL data to improve the fit with the GIA model predictions in each region. To
344 allow for shorter-term variability resulting from centennial-scale earthquake deformation cycles, we

include a ± 1 m envelope around the model predictions. The magnitude of this envelope provides a conservative assessment of centennial cycles, reflecting the upper bound of vertical deformation recorded at coastal sites during 20th and 21st century great earthquakes (Plafker and Savage, 1970; Farías et al., 2010; Klein et al., 2017). We accept all corrections that result in index points (including error terms) overlapping the suite of model predictions, terrestrial limiting points sitting within or above the predictions, and marine limiting points lying within or below the predictions.

4. New sea-level data

In addition to compiling and standardising sea-level data from the literature (section 5), we present four new sea-level data points from hitherto unstudied sites.

4.1 Pelluhue, Maule region

At Pelluhue (35.8133°S 72.5762°W), an outcrop at the landward edge of the contemporary beach exposes an abrasion platform carved into metamorphic bedrock. Black volcanic sand and a colluvial wedge overlie the platform (Fig. 2). The medium to coarse volcanic sand is similar in composition and grain size to the contemporary beach sand but lacks datable organic material. The colluvium consists of angular pebbles, rounded cobbles and charcoal fragments that we interpret as having accumulated above the reach of tides. We radiocarbon dated three charcoal fragments from a layer at the base of the colluvium at an elevation of 4.87 ± 0.15 m MSL. The resulting dates constrain the timing of the deposition of the colluvium; the median calibrated ages lie within 100 years of each other (Table 2). The youngest calibrated age range, 4407 – 4095 cal a BP, provides the age for a terrestrial limiting point. We derive the maximum elevation of RSL by taking the reference water level (HAT = 1.08 m) away from the sample elevation and adding the sum of the positive vertical uncertainties (comprising uncertainties related to the absolute elevation, the depth within the

section, and the indicative meaning: 0.19 m). The terrestrial limiting point therefore indicates RSL was below 3.98 m.

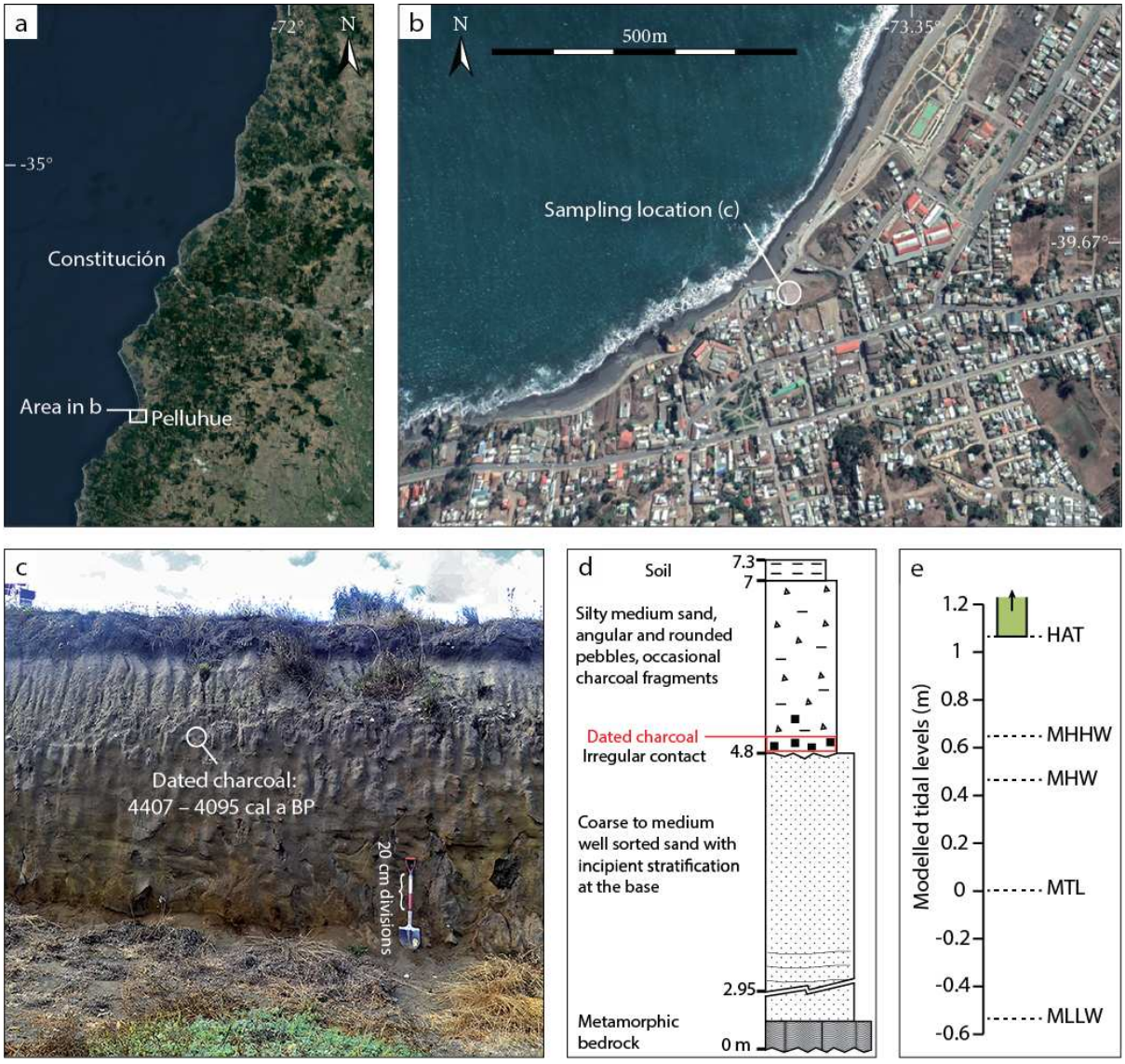

Figure 2: Derivation of the new terrestrial limiting point from Pelluhue. a) Location of Pelluhue and b) sampling location. c) Photograph and d) stratigraphic log of the dated section. e) Graphical representation of the terrestrial limiting point's indicative meaning (open-ended green box; above highest astronomical tide) relative to tidal levels at the site modelled using the TPXO8-ATLAS tidal model (Egbert and Erofeeva, 2010). Basemaps in a) and b) are from Bing Maps.

Table 2: Radiocarbon data associated with the new sea-level data points from Pelluhue, Tubul, Punta Pájaros Niños, and Pilolcura. Reported ages are conventional ^{14}C ages in years before 1950 CE, corrected for isotopic fractionation using $\delta^{13}C$ (NR = $\delta^{13}C$ not reported). Ages calibrated with OxCal 4.2 (Bronk Ramsey, 2009) and the SHCal13 calibration curve (Hogg et al., 2013), except for the calibrated range marked *, which are calibrated using the Marine13 calibration curve (Reimer et al., 2013) and ΔR = 137 ± 164 years, as discussed in section 3.5.

Sample name	Laboratory code	Sample elevation (mMSL)	Dated material	$\delta^{13}C$	^{14}C years BP ± 1σ	Calibrated age (years BP, 2σ)
Pelluhue						
PEL001	Poz-50368	4.87 ± 0.15	Charcoal fragment	-23.8	3925 ± 35	4420 – 4158
PEL002	Poz-50369	4.87 ± 0.15	Charcoal fragment	-25.5	3890 ± 35	4412 – 4150
PEL003	Poz-50370	4.87 ± 0.15	Charcoal fragment	-25.0	3870 ± 35	4407 – 4095
Tubul						
TUB001	Beta-276181	2.72 ± 0.13	*Petricola rugosa* shell	-0.5	4780 ± 40	5302 – 4421*
Punta Pájaros Niños, Isla Mocha						
PPN001	KIA 36874	21.9 ± 0.20	*Leukoma thaca* shell	-1.1	3625 ± 30	3790 – 2934*
Pilolcura						
PIL001	D-AMS 032803	2.47 ± 0.07	Charcoal fragment	NR	1161 ± 36	1089 – 932

4.2 Tubul, Arauco region

One kilometre north of the mouth of the Río Tubul (37.2265°S 73.4357°W), a partially exhumed wave-cut bedrock platform, cut into siltstone from the Plio-Pleistocene Tubul Formation, lies above present sea level (Fig. 3). The surface of the platform is heavily pitted by the subtidal to low intertidal rock-boring bivalves *Petricola rugosa*, *Petricola dactylus* and *Pholas chiloensis.* A poorly consolidated clast-supported conglomerate containing subrounded bivalve-bored mudstone and sandstone cobbles and boulders, gravel, articulated and fragmented subtidal clams (*Leukoma thaca*), marine gastropods (*Turitella* sp.), charcoal fragments, and a sand-rich matrix locally overlies the platform. We hypothesise that this conglomerate results from the debris from a landslide from the adjacent cliffs that was subsequently reworked by waves. We base this assumption on our observations of similar effects seen after the 2010 earthquake, which triggered a landslide above the

studied site. Since 2010, we have observed how storm waves have reworked the resulting landslide debris.

We dated an articulated *Petricola rugosa* shell found in life position inside its hole in the bedrock platform, which was preserved beneath the conglomerate (Table 2). As living *P. rugosa* individuals are found beneath MTL and generally in water depths of less than 10 m (Bernard, 1983), the resulting calibrated date, 5302 – 4421 cal a BP, provides the age of a marine limiting point. Accounting for the sample elevation (2.69 m), the reference water level (MTL = -0.01 m), and the sum of the negative vertical uncertainties (0.13 m), the limiting point indicates RSL above 2.57 m.

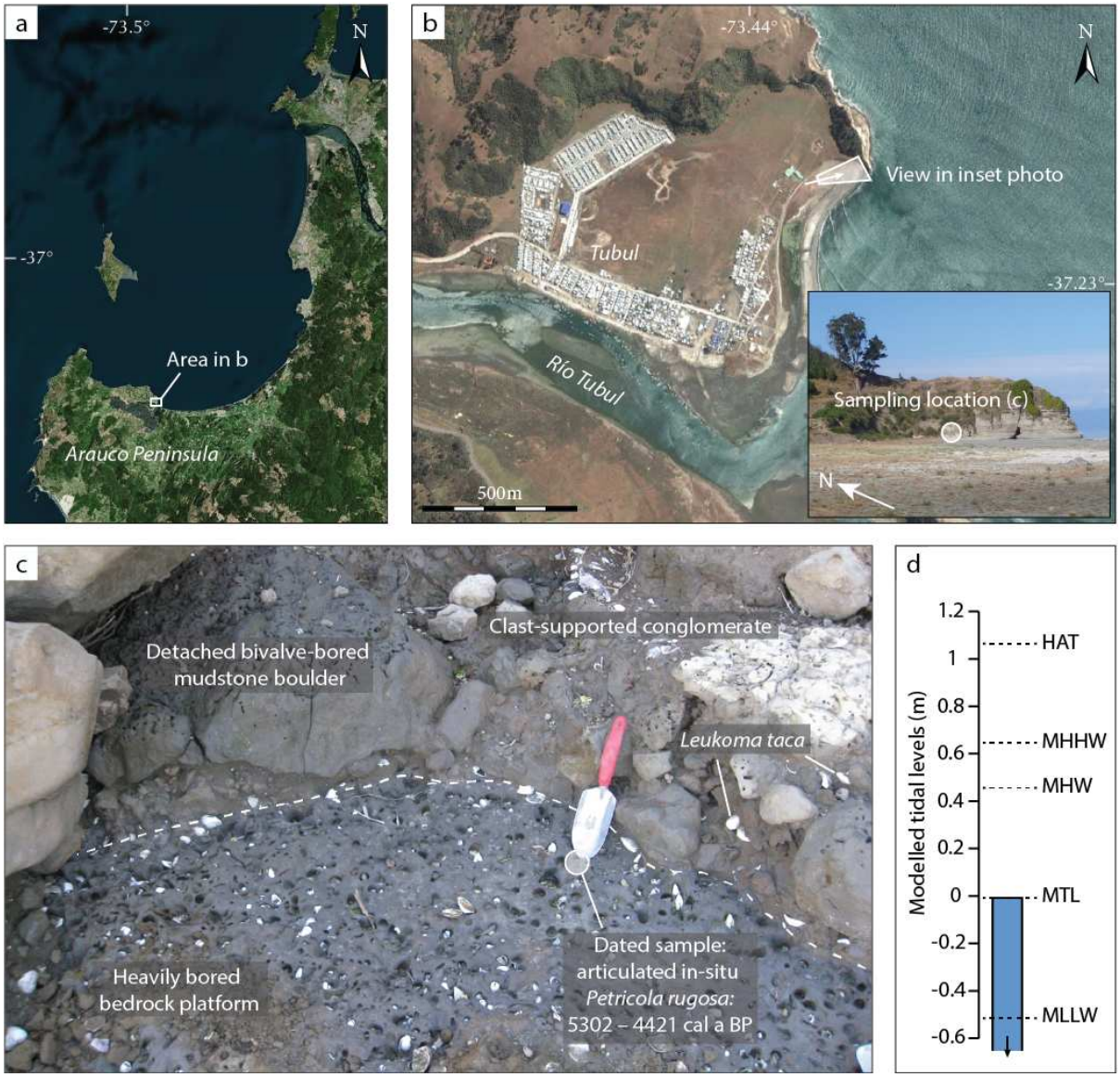

Figure 3: Derivation of the new marine limiting point from Tubul. a) Location of Tubul on the northern side of the Arauco Peninsula, b) sampling location on the headland east of Tubul, c) photograph of the bivalve-bored bedrock platform with the location of the dated *Petricola rugosa*, d) graphical representation of the marine limiting point's indicative meaning (open-ended blue box; below mean tide level) relative to tidal levels at the site modelled using the TPXO8-ATLAS tidal model (Egbert and Erofeeva, 2010). Basemaps in a) and b) are from Bing Maps.

4.3 Punta Pájaros Niños, Isla Mocha

Towards the northernmost point of Isla Mocha, at Punta Pájaros Niños (38.3250°S 73.9549°W), we encountered a coquina layer at an elevation of ~22 m (Fig. 4). The coquina contains bivalves (*Leukoma thaca*) and gastropods (*Tegula atra* or *Diloma nigerrimum*), with a poorly cemented sandy matrix. The high proportion of shell material and the presence of multiple marine species of differing environmental preference, including subtidal species from sandy substrates and intertidal species from rocky substrates, suggests reworking and deposition in a high-energy subtidal or possibly intertidal environment. The layer lacks any morphological evidence for supratidal deposition in the form of a beach ridge or shell midden, while the low gradient of the site substantially reduces the possibility of post-depositional reworking. The thin overlying conglomerate is of fluvial origin, with very well-rounded andesite clasts implying connectivity with the mainland or possibly reworking from higher elevations, although the latter hypothesis appears less likely given the site morphology. A whole, although not articulated, *Leukoma thaca* shell provides an age for the coquina of 3790 – 2934 cal a BP (Table 2). As the water depth at which coquina deposits form is unknown in this setting, we conservatively treat the sample as a marine limiting point with an indicative range of below HAT. Taking away the reference water level (HAT = 1.09 m) and the sum of the negative vertical uncertainties (0.24 m) from the sample elevation (21.90 m) indicates RSL was above 20.57 m.

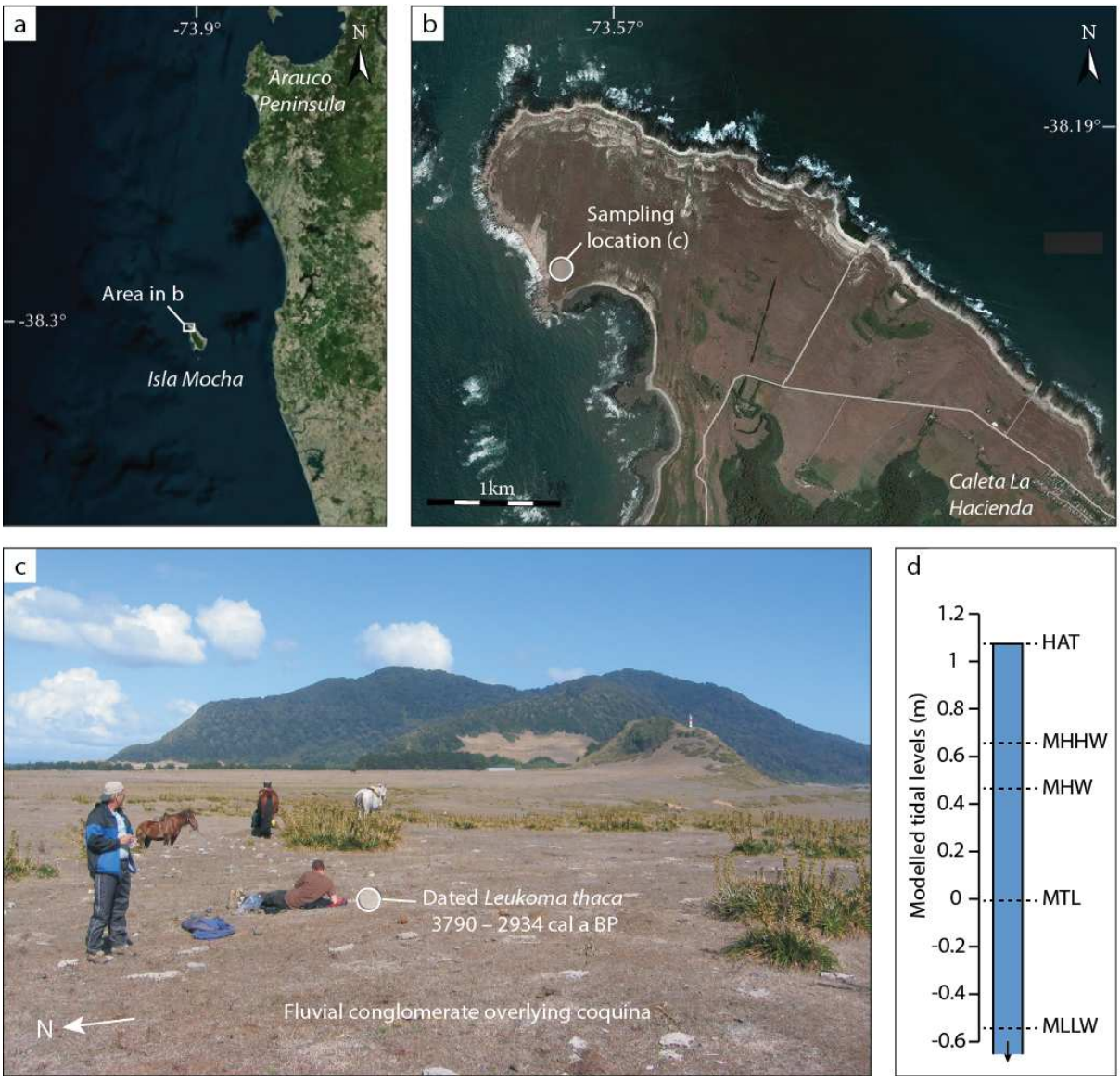

Figure 4: Derivation of the new marine limiting point from Punta Pájaros Niños. a) Location of Isla Mocha and b) the sampling location close to the northern tip of the island. c) Photograph of the sampling site, d) graphical representation of the marine limiting point's indicative meaning (open-ended blue box; below highest astronomical tide) relative to tidal levels at the site modelled using the TPXO8-ATLAS tidal model (Egbert and Erofeeva, 2010). Basemaps in a) and b) are from Bing Maps.

4.4 Pilolcura, Valdivia region

447

448 At Pilolcura (39.6723°S 73.3519°W), a ~1.8 m high section at the landward edge of the contemporary
449 beach exposes a mid to dark grey silt-rich sand underlying ~1.2 m of colluvium (Fig. 5). The silt-rich
450 sand contains a diatom assemblage dominated by freshwater or salt tolerant taxa (*Karayevia*
451 *oblongella* and *Humidophila contenta*). The presence of infrequent brackish (e.g. *Luticola mutica*)
452 and occasional marine species (e.g. *Petroneis marina*) suggests an environment with some tidal
453 influence. The combination of a mixed-salinity diatom assemblage and fine-grained clastic sediments
454 may indicate a tidally influenced lagoon behind a barrier or spit. Comparison of the fossil diatom
455 assemblages with the contemporary distribution of intertidal diatoms in >250 samples from south-
456 central Chile (Hocking et al., 2017) indicates a depositional elevation between MHHW and HAT
457 (Supplementary Information S2). Nevertheless, the modern diatom database does not provide a
458 close analogue for the Pilolcura assemblage, and we consequently assign a more conservative
459 indicative range of between MTL and HAT (Fig. 5e). A fragment of charcoal at a depth of 1.50 m
460 provides a calibrated radiocarbon age of 1089 – 932 cal a BP (Table 2). Taking the reference water
461 level (midpoint between MTL and HAT: 0.55 m) away from the sample elevation (2.47 m), we infer
462 sea level was at 1.92 m. The vertical uncertainty for this index point (0.57 m) is the sum of the
463 uncertainties related to the absolute elevation, the depth within the exposure, and the indicative
464 meaning.

465

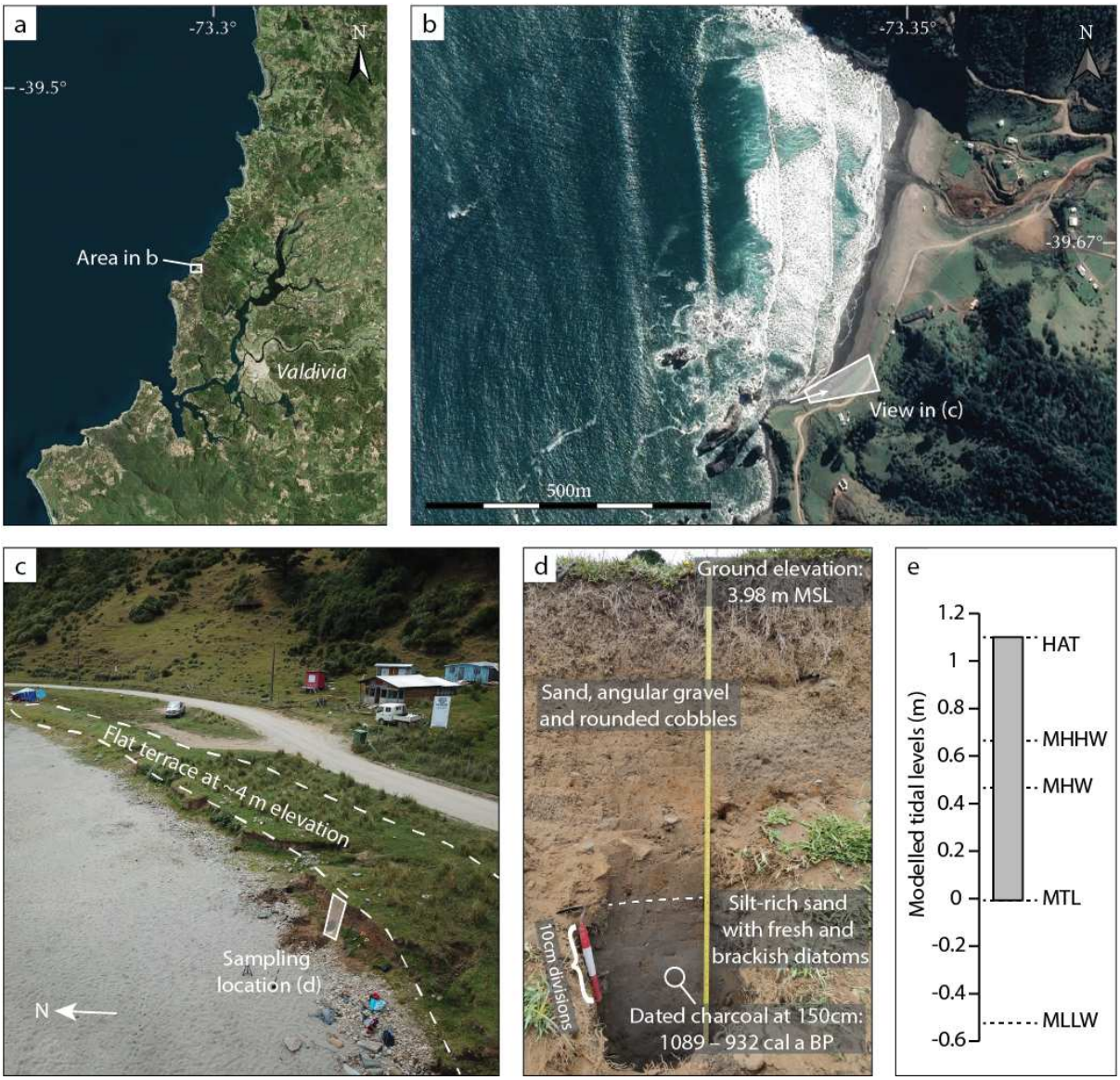

Figure 5: Derivation of the new sea-level index point from Pilolcura. a) – c) Location of the sampling site, d) photograph of the dated section, e) graphical representation of the index point's indicative meaning (grey box; between mean tide level and highest astronomical tide) relative to tidal levels at the site modelled using the TPXO8-ATLAS tidal model (Egbert and Erofeeva, 2010). Basemaps in a) and b) are from Bing Maps.

5. The database and regional sea-level histories

The Chilean Holocene RSL database (accessible via the data repository) consists of 166 accepted points, of which 79 are index points, 56 are terrestrial limiting points, and 31 are marine limiting points (Fig. 6). We reject a further 53 points for a range of reasons including uncertainties over depositional environments, the possibility of reworking by storms, rivers, tsunamis, or human activity, and chronological outliers identified by the original or subsequent authors. Of the accepted points, 45 are from basal settings, including 28 index points, with the remaining 121 intercalated. Almost 40 % of the accepted points have median ages postdating 1 ka BP, while only 10 points (6 %), nine of which are marine limiting, are older than 6.5 ka BP (Fig. 6). In figure 7, we present sea-level histories for the 11 regions shown in figure 1.

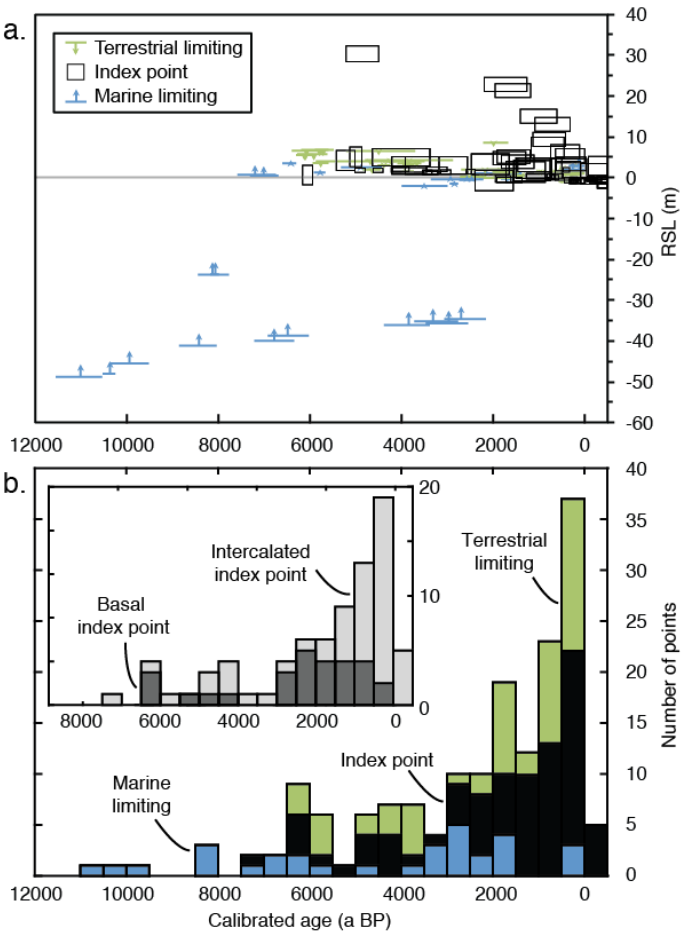

Figure 6: a. Plot of all accepted sea-level data points in the Chilean database. b. Stacked histogram of the temporal distribution of accepted sea-level data points. Inset compares the distribution of basal and intercalated sea-level index points.

489

490 5.1 Antofagasta (Fig. 7, region 1)

491

492 The coastline bordering the arid Atacama Desert, covering more than 10 degrees of latitude,
493 currently provides a single Holocene marine limiting point. Leonard and Wehmiller (1991) report
494 three uplifted marine terraces at Caleta Michilla, with only the lowermost having formed during the
495 Holocene. Marine bivalves from this terrace, lying at an elevation of approximately 5.5 m above
496 mean sea level, provide a median age of ~7.2 ka BP. While the authors describe the dated sediments
497 as marine, it is unclear whether the terrace is a raised beach deposited at or above HAT, or a marine
498 deposit with a lower indicative range. Consequently, we consider this sample as a marine limiting
499 point with a reference water level of HAT + 3 m. Our interpretation places RSL above ~0.5 m at this
500 time.

501

502 5.2 Coquimbo and Tongoy (Fig. 7, region 2)

503

504 The RSL record of this semi-arid region consists of 11 index points and one marine limiting point
505 from five sites. In contrast to the paucity in other regions, 9 of the 11 index points are from basal
506 settings. The earliest sea-level data point, a ~7.2 ka BP marine limiting point from Estero Tongoy (Ota
507 and Paskoff, 1993), places sea level above ~0.7 m. Index points from prograding sequences of beach
508 ridges in the Bay of Coquimbo (Hart et al., 2017) and beach deposits at El Rincón and Punta Lengua
509 de Vaca, both fringing Tongoy Bay (Ota and Paskoff, 1993), indicate falling sea level after ~5 ka BP
510 from a maximum of at least 5.00 ± 2.09 m. Three index points from Puerto Aldea and El Rincón (Ota
511 and Paskoff, 1993) indicate RSL was between 0 m and 5 m by 2 ka BP, with the large vertical
512 uncertainty associated with the broad indicative range associated with index points from
513 undifferentiated beach environments. Within the last 100 years, two index points from Quebrada de
514 Teatinos, Bay of Coquimbo, place RSL around -1.8 m, with a vertical uncertainty of ~0.7 m (May et

al., 2013). We do not incorporate further dated samples from Quebrada Los Chines (Ota and Paskoff, 1993), Quebrada de Teatinos, and Quebrada Pachingo (May et al., 2013) due to the potential for reworking or chronological uncertainties identified by the original authors.

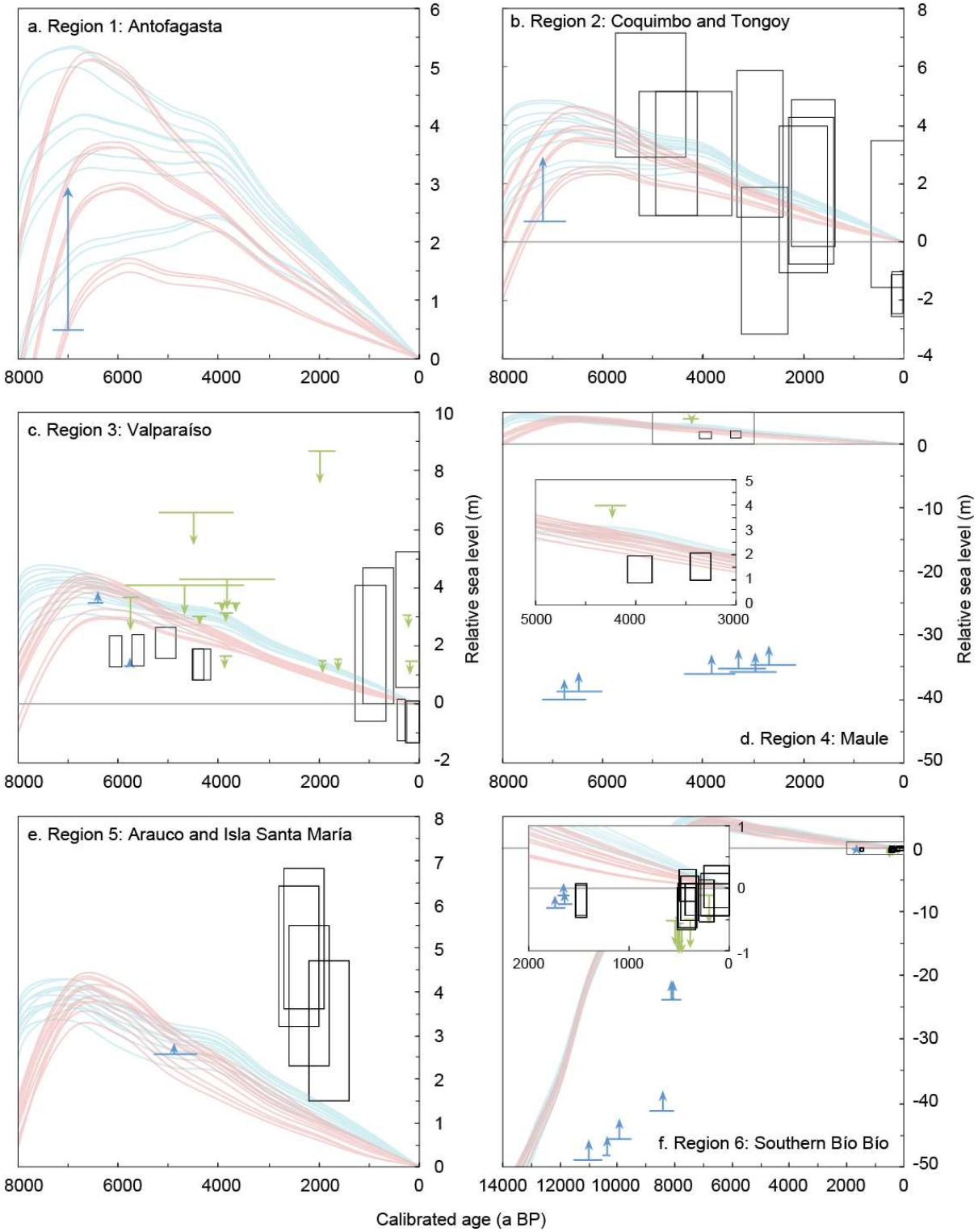

Figure 7: Regional plots comparing the age – elevation distribution of the sea-level data points with glacial isostatic adjustment model predictions (following Peltier, 2004; Peltier et al., 2015). Sea-level index points are black rectangles, terrestrial and marine limiting points are green T-shaped symbols and blue ⊥-shaped symbols respectively. ICE_5G predictions are light blue curves, ICE_6G predictions are pink curves; for both ice models, we vary the lithospheric thickness between 71 and 120 km and the upper mantle viscosity between 5 x 10^{19} Pa s and 2 x 10^{20} Pa s (see section 3.7). Note different x-axis scaling for panel f and variable y-axis scaling between all panels.

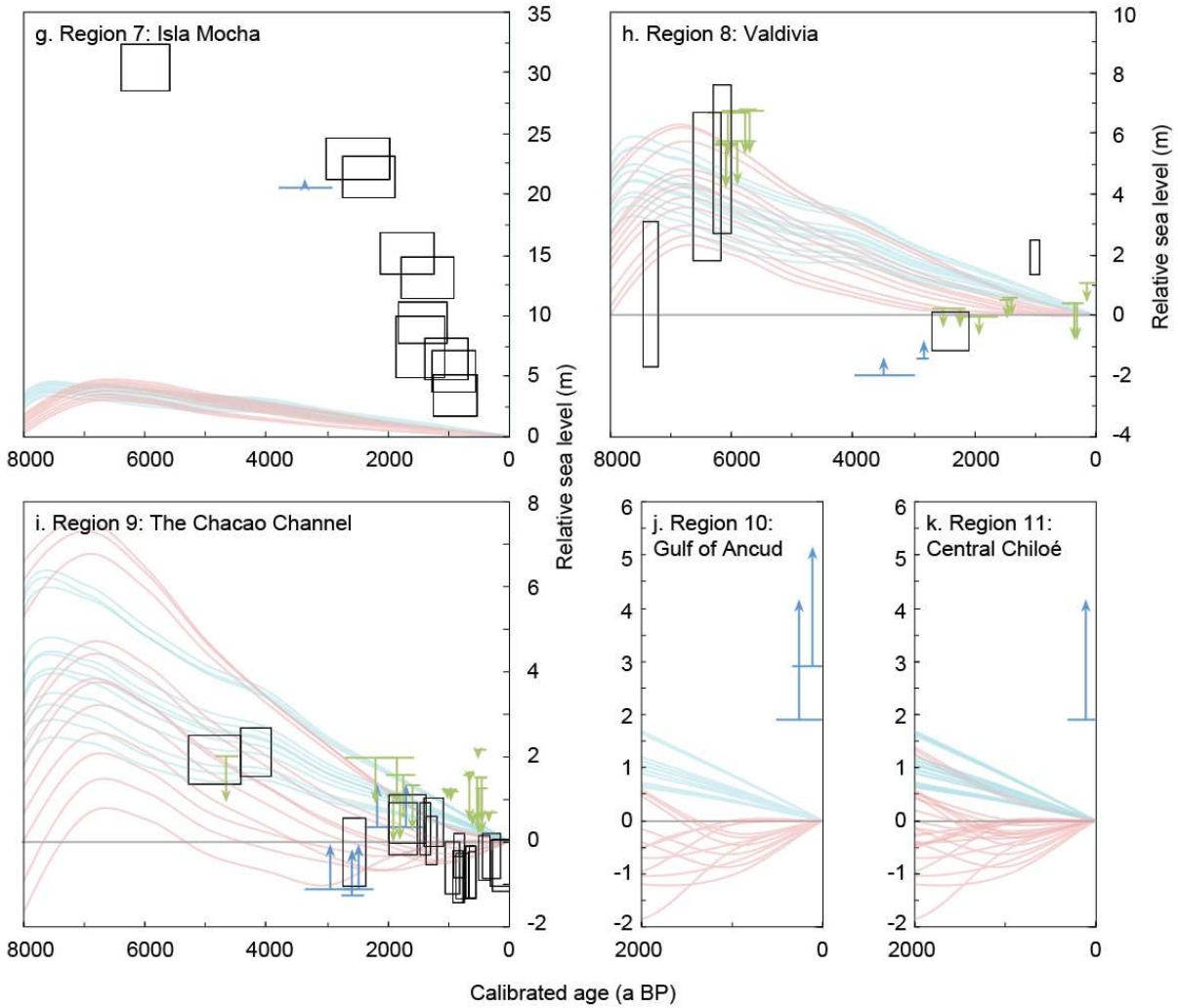

Figure 7 (continued)

5.3 Valparaíso (Fig. 7, region 3)

Five sites in the Valparaíso region provide 11 index points, 2 marine limiting and 14 terrestrial limiting points. The earliest evidence comes from Algarrobo, where Encinas et al. (2006) report a silty sandstone containing well-preserved foraminifera, bivalves and gastropods, indicative of a shallow marine environment. This marine limiting point places RSL above ~3.5 m at ~6.4 ka BP. Tidal and freshwater marsh deposits at Quintero, originally investigated for their palaeotsunami record (Dura et al., 2015), provide mid Holocene index points and late Holocene terrestrial limiting points. These data indicate sea level was ~2 m at ~6 ka BP, below 1.65 m at ~3.9 ka BP, and below ~1.5 m during the last 2 ka. Terrestrial limiting points from alluvial deposits underlying the Longotoma dune field concur, indicating sea level below ~3.5 m at ~4 ka BP (May et al., 2015). Within the last millennium, index points from Los Vilos (May et al., 2013) indicate RSL above present, though with large vertical uncertainties, while index points from Pichicuy Bay (May et al., 2013) indicate RSL between -1.3 and 0.2 m.

5.4 Maule (Fig. 7, region 4)

In addition to the new terrestrial limiting point from Pelluhue (section 4.1), the sea-level history of this region is further constrained by two index and six marine limiting points from two sites. Frugone-Álvarez et al. (2017) report 11 radiocarbon dates from cores taken from Lago Vichuquén. The lowermost six samples are from sediments interpreted by Frugone-Álvarez et al. (2017) as indicative of marine environments; consequently, the dates constrain the ages of marine limiting points. As the location and elevation of the sill between the lake basin and the sea at the time of deposition is uncertain (today it lies at 2.4 m above EGM2008), we conservatively assume that there was no sill. The accepted marine limiting points place RSL above -40 m at ~6.8 ka BP and above -35 m at ~2.7 ka BP. While the overlying sediments are interpreted as brackish and freshwater (Frugone-Álvarez et al., 2017), radiocarbon dates from these layers cannot be used to constrain sea level due to uncertainties over the isolation of the lake and the role of sediment supply and local

558 tectonics in building the sill. The terrestrial limiting point from Pelluhue places RSL below ~4 m at
559 ~4.2 ka BP, while two index points from El Yolki indicate RSL between 0.85 and 2.1 m between 4 and
560 3 ka BP (Hilleman, 2015; Melnick et al., 2019). We do not consider 13 other radiocarbon dates of
561 ~4 ka BP from Melnick et al. (2019) due to their close proximity to the El Yolki Fault.
562
563 5.5 The Arauco Peninsula and Isla Santa María (Fig. 7, region 5)
564
565 The RSL record consists of four basal index points from Isla Santa María and the new marine limiting
566 point from Tubul. The eastern side of Isla Santa María features a sequence of 21 emerged Holocene
567 beach ridges at elevations between 0.5 m and 8 m. Optically stimulated luminescence ages constrain
568 the timing of the deposition of four of the ridges to the late Holocene, with the oldest dating to 2.1 –
569 2.5 ka BP (Bookhagen et al., 2006). We use the elevation of these four ridges at the locations at
570 which they were sampled for dating to define four index points, noting that the ridges are
571 progressively tilted to the northwest at a rate estimated by Bookhagen et al. (2006) of
572 0.022 ± 0.002 °/ka. These index points place RSL between 3.11 m and 5.21 m, with vertical
573 uncertainties of ± 1.6 m. As described in section 4.2, a marine limiting point from Tubul places sea
574 level above 2.57 m at ~5 ka BP.
575
576 Although two shells have been dated on the coastal plains at Coronel and Carampangue (Isla et al.,
577 2012), we are unable to derive index or limiting points. Because both dates relate to broken shells of
578 unknown species, we cannot establish whether these shells are originally from subtidal, intertidal or
579 supratidal environments and whether they are in-situ or have been subsequently transported.
580
581 5.6 Southern Bío Bío (Fig. 7, region 6)
582

583 The RSL history of the Southern Bío Bío region is constrained by 10 index, 8 terrestrial limiting, and 9
584 marine limiting points. We derive two marine limiting points from Lake Lanalhue and four marine
585 limiting points from Lake Lleu Lleu (Stefer et al., 2010). The dated samples, ranging from 8 to 11 ka
586 BP, come from clastic sediments containing marine shells and foraminifera at elevations of between
587 -22 m and -47 m. While the basins also contain subsequent lacustrine sedimentary infills, we cannot
588 derive terrestrial limiting points from 17 further radiocarbon dates from these intervals due to the
589 uncertain rate of tectonic uplift and coeval erosion of the sill that separates the contemporary lake
590 from the Pacific. Organic silt and peat layers at Quidico (38.2°S) and Tirúa (38.3°S) provide 21 further
591 sea-level data points, including 10 index points (Ely et al., 2014; Dura et al., 2017; Hong et al., 2017).
592 The accepted ages are all within the last 1.9 ka and lie between -0.6 m and 0.4 m.
593
594 5.7 Isla Mocha (Fig. 7, region 7)
595
596 Ten index points, all of them from basal settings, and one marine limiting point constrain the sea-
597 level history of Isla Mocha. The island, lying approximately 30 km off the coast of mainland Chile,
598 features a kilometre-wide fringe of uplifted Holocene beach ridges (Nelson and Manley, 1992). Two
599 studies provide radiocarbon ages from either shell fragments or intact shells from beach ridges at
600 elevations up to 33 m (Kaizuka et al., 1973; Nelson and Manley, 1992). Following Nelson and Manley
601 (1992), we exclude several of these ages due to the probability of reworking of older shell material.
602 The 10 accepted index points, along with our new marine limiting point from the north of the island
603 at Punta Pájaros Niños, place RSL around 30 m at ~6 ka BP, falling to ~23 m at ~2.5 ka BP and
604 subsequently falling at a faster rate to below 5 m at ~0.9 ka BP.
605
606 5.8 Valdivia (Fig. 7, region 8)
607

608 Five index, two marine limiting and 14 terrestrial limiting points provide the RSL record for the
609 Valdivia region. The oldest index point, coming from shell-bearing sands indicative of a beach
610 environment at Isla Mancera (Villalobos Silva, 2005), dates to ~7.3 ka BP and places RSL between -
611 1.7 m and 3.1 m, with the large vertical uncertainty reflecting a broad indicative range. Index points
612 from beach sediments and terrestrial limiting points from aeolian dunes at Chan Chan indicate RSL
613 was between 1.8 m and 7.6 m at ~6 ka BP (Pino and Navarro, 2005). Between ~3.5 ka BP and
614 present, index and marine limiting points from tidally influenced clastic sediments and terrestrial
615 limiting points from freshwater soils in the Las Coloradas inlet and Isla Mancera place RSL between -
616 2 m and 1 m (Villalobos Silva, 2005; Nelson et al., 2009). The new index point from Pilolcura places
617 RSL at 1.92 ± 0.57 m, ~1 ka BP.
618
619 5.9 The Chacao Channel (Fig. 7, region 9)
620
621 The coast of northern Chiloé and the adjacent continental coast around the Río Maullín, collectively
622 termed the Chacao Channel region, provide 26 index, five marine limiting and 19 terrestrial limiting
623 points. These points stem from palaeoseismic studies of coastal lowlands and marshes (Atwater et
624 al., 1992; Cisternas et al., 2005; 2017; Garrett et al., 2015). The earliest sea-level data come from
625 Chocoi, where tidal marsh peat layers exposed in a sea cliff attest to RSL ~2 m above present
626 between 5 and 4 ka BP (Atwater et al., 1992). A subsequent fall in RSL is recorded by tidal marsh
627 deposits at Maullín (Cisternas et al., 2005), Dadi, and Puente Cariquilda (Atwater et al., 1992). Six
628 index points from these locations place RSL between -1 m and 1 m during the period between 3 and
629 1 ka BP. Terrestrial limiting points in this interval place sea level below 2 m, with marine limiting
630 points indicating sea level above -1.5 m at ~3 ka BP and above 0.35 m at ~2 ka BP. Twelve index
631 points from Chucalen (Garrett et al., 2015) and six from Maullín (Cisternas et al., 2005) indicate RSL
632 was ~1 m below present at ~0.9 ka BP, with the subsequent rise to present overprinted by metre-
633 scale coseismic subsidence events resulting from great subduction earthquakes (Garrett et al.,

2015). Terrestrial limiting points for the last 1 ka from Maullín (Cisternas et al., 2005) and Cocotué (Cisternas et al., 2017) indicate sea level below elevations varying between 2.3 m and 0.7 m.

5.10 Reloncaví Sound and Gulf of Ancud (Fig. 7, region 10)

Two marine limiting points constrain the RSL history of the semi-enclosed coastlines to the northeast of Chiloé. Both points come from Bahía Hualaihué, where intertidal or subtidal bivalves in living position indicate sea levels above 1.90 m and 2.90 m (Hervé and Ota, 1993). Both samples have median ages within the last 0.3 ka. We reject further dated shells from Bahía Hualaihué and sites at Ralún at the head of Fiordo Reloncaví and the Cholgo Canal (Hervé and Ota, 1993) due to the possibility of reworking by extreme waves or human activity.

5.11 Central Chiloé (Fig. 7, region 11)

Central Chiloé provides a single marine limiting point, with no further accepted sea-level data from southern Chiloé, Isla Guafo or the continental coastline or islands of the Gulf of Corcovado. At Cucao, on the western coast of Chiloé, Hervé and Ota (1993) report subtidal bivalves in living position indicating RSL above 1.89 m. Recalibration of the radiocarbon age provides a range of 325 cal a BP to present. We reject one dated shell from Nercón on the eastern coast of Chiloé (Hervé and Ota, 1993) due to the possibility of reworking.

6. Discussion

6.1 Glacial isostatic adjustment

659 The Chilean sea-level database includes 166 accepted sea-level data points. Nevertheless, as these
660 are unevenly spread across 2200 km of coast (20 degrees of latitude), our current knowledge of past
661 sea levels is spatially variable and, in some areas (regions 1, 4, 10, 11, and all remaining stretches of
662 coastline that lack any data), highly limited. Nonetheless, the presence of several data-rich regions
663 with well-constrained sea-level histories highlights a high degree of spatial variability in Holocene
664 RSL change and provides an opportunity to make a preliminary investigation into the processes
665 driving these changes. To this end, we compare the distribution of sea-level data with RSL
666 predictions from a suite of GIA models (Fig. 7).
667
668 GIA model predictions display a high degree of variability along the Chilean coastline. The two
669 northernmost regions are characterised by modelled mid Holocene highstands 1.5 – 5.5 m above
670 present between 7 ka and 4 ka (Fig. 7a-b). The five central regions between Valparaíso and Isla
671 Mocha share modelled highstands 3 – 6 m above present at 7 ka or 6 ka (Figs. 7c-g). The predictions
672 for the four southernmost regions, around Valdivia and Isla de Chiloé, display maxima at elevations
673 between 0.5 and 8 m above present at 8 ka or 7 ka, with a high degree of variability between
674 different models (Figs. 7h-k). Unlike in regions 1 – 8, where all models predict RSL fall following the
675 highstand, models that adopt low values for upper mantle viscosity, when combined with the ICE-6G
676 ice model, predict RSL rise over the last 1 – 3 ka in regions 9 – 11 (Figs. 7i-k).
677
678 For the majority of Chilean regions, the database of sea-level data points and the GIA model
679 predictions provide a coherent account of the pattern of Holocene RSL change. No additional factors
680 are required to explain the age and elevation of data points in regions 1 and 4 (Fig. 7); however, this
681 may reflect the paucity of data in these regions. In regions 2, 3, 6, 8, and 9, decimetre- to metre-
682 scale vertical motions associated with centennial-scale earthquake cycle deformation would be
683 sufficient to account for the small disparities between sea-level data and GIA model predictions. In
684 the remaining regions—Arauco and Isla Santa María (region 5), Isla Mocha (region 7), the Gulf of

685 Ancud (region 10), and Central Chiloé (region 11)—index and marine limiting points consistently lie
686 above the GIA predictions, suggesting the importance of other factors at these locations. In the
687 following section, we explore the potential for millennial-scale secular tectonic uplift to account for
688 these differences.
689
690 6.2 Regional tectonic uplift
691
692 Allowing for centennial-scale earthquake deformation cycles, we apply linear corrections to the RSL
693 data to improve the fit with the GIA model predictions (see section 3.7 and Supplementary
694 information S3). We summarise the range of acceptable linear corrections for each region in Figure 8
695 and compare these with independently derived estimates of multi-millennial-scale tectonic uplift.
696 We note that our linear corrections provide a first approximation of tectonic uplift rates, but also
697 reflect the cumulative effects of other processes including sediment compaction and sediment
698 isostasy, among other local processes. We make an initial exploration of the possible role of tectonic
699 uplift and other processes in each region in the following paragraphs.
700
701 As previously stated, once centennial-scale deformation cycles are accounted for, no additional
702 correction is required to explain data-model discrepancies in regions 1, 2, 3, 4, 6, 8, and 9. However,
703 a range of positive and/or negative corrections may still provide acceptable fits with the model
704 predictions. In regions 1 and 2, our accepted ranges of linear corrections (>-0.8 m ka^{-1} and -0.3 –
705 0.6 m ka^{-1} respectively) overlap with Melnick's (2016) independent estimates based on a landscape
706 evolution model for the central Andean rasa (Fig. 8). In region 3, as mid-Holocene index points lie
707 below GIA model predictions, we invoke negative rates of -0.3 to 0 m ka^{-1} (subsidence) (Fig. 8). The
708 slight discrepancy between this and Melnick's (2016) tectonic uplift rate of 0.06 ± 0.02 m ka^{-1} could
709 indicate sediment compaction affects the intercalated index points from the organic-rich lowland at
710 Quintero (Dura et al., 2015).

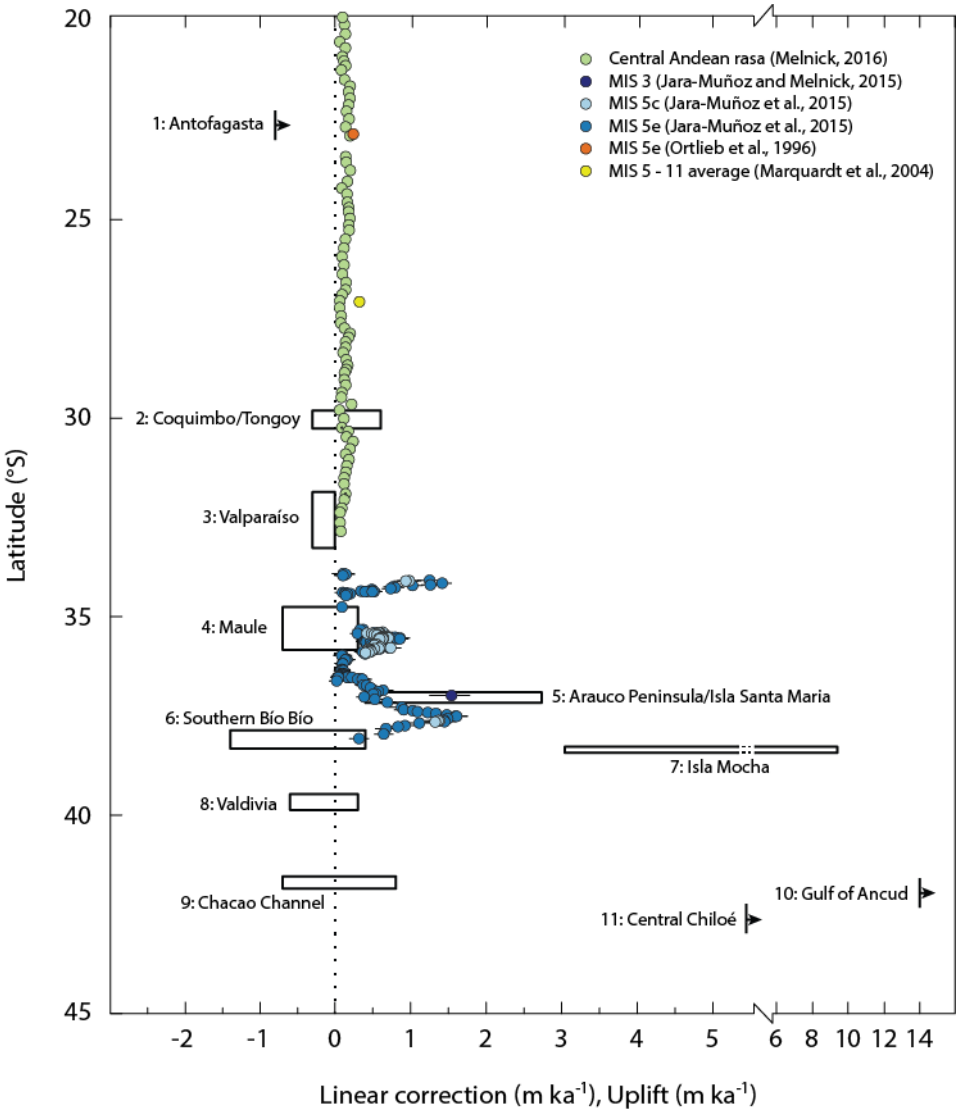

Figure 8: Comparison of best-fit linear correction rates (black rectangles) required to remove the misfit between sea-level data and a suite of glacial isostatic adjustment models with independently derived estimates of tectonic uplift (coloured circles). Sea-level data and GIA models for the 11 regions are shown in Figure 7 and the linear corrections are illustrated in Supplementary Information S3.

Accepted linear correction rates for region 4 range from -0.7 m ka^{-1} (subsidence) to 0.3 m ka^{-1} (uplift) (Fig. 8). Jara-Muñoz et al. (2015) suggest higher tectonic uplift rates in the region since the last interglacial, with rates of 0.4 to 0.8 m ka^{-1} associated with a long-wavelength upwarping zone and

722 the activity of three major crustal normal faults that intersect the coastline and displace the marine
723 isotope stage (MIS) 5 marine terraces. Correcting the sea-level data for such high tectonic uplift rates
724 would lower index points below our model predictions. This could 1) potentially indicate a greater
725 level of spatial variability in uplift rates associated with local crustal structures than previously
726 identified, 2) suggest that late Holocene tectonic uplift rates have not been sustained over longer
727 timescales, or 3) reflect spatial complexity in Earth rheology that is not accounted for by GIA models.
728 Uplift rates inferred from last interglacial terraces do not account for local departures from the
729 global eustatic sea level associated with GIA (Creveling et al., 2015), potentially also contributing to
730 the disparity with the inferred Holocene rates.
731
732 A linear correction of between 0.4 and 2.7 m ka^{-1} (uplift) could account for the elevated position of
733 the four index points from Isla Santa María with respect to the GIA model predictions for region 5
734 (Figs. 7e, 8). Jara-Muñoz and Melnick (2015) concur, inferring a tectonic uplift rate of 1.5 ± 0.3 m ka^{-1}
735 from MIS 3 sediments on Isla Santa María. We note that continued debate over MIS 3 sea levels may
736 lead to a reassessment of this rate (Pico et al., 2017; Dalton et al., 2019). Jara-Muñoz et al. (2015)
737 indicate lower post-MIS 5e tectonic uplift rates for the Arauco Peninsula, including ~0.3 m ka^{-1} at the
738 latitude of our site at Tubul. Neither the MIS 5e nor the MIS 3 uplift rates account for local GIA-
739 induced departures from global eustasy (Creveling et al., 2015).
740
741 Linear corrections of -1.4 m ka^{-1} (subsidence) to 0.4 m ka^{-1} (uplift) provide the best fit for the late
742 Holocene in region 6 (Fig. 8). Based on comparison of the early Holocene record from lakes Lanalhue
743 and Lleu Lleu with "global" sea-level curves, Stefer et al. (2010) inferred tectonic uplift rates in the
744 region of 0.5 m ka^{-1}. We update this analysis by comparing reassessed sea-level data from the two
745 lakes with the suite of GIA model predictions for this particular location. As a result of isostatic
746 rebound, the model predictions for this region lie substantially above farfield RSL curves, implying
747 that the uplift rates derived in the original study were overestimated. While the Lanalhue and Lleu

748 Lleu marine limiting points lie above the global curves (Stefer et al., 2010), they lie below the local
749 model predictions (Fig. 7f and supplementary figure S3f). Consequently, no tectonic uplift is required
750 to reconcile the observations of Stefer et al. (2010) with the model predictions, in contrast to the
751 conclusions of the original study.
752
753 Sea-level index points from Isla Mocha lie above the suite of GIA model predictions for region 7 (Fig.
754 7g). Linear corrections of between 3 m ka^{-1} and 9.5 m ka^{-1} reduce the misfit, with the highest uplift
755 rates required to reconcile data from the last 3000 years (Fig. 8). No single rate can bring every index
756 point within the suite of model predictions, potentially indicating an increase in uplift rates during
757 the Holocene, as identified by Nelson and Manley (1992). The rapid localised tectonic uplift of Isla
758 Mocha, contrasting with the adjacent southern Bío Bío region, may reflect aseismic and/or seismic
759 slip on imbricate thrust faults within the South American Plate (von Heune et al., 1985; Nelson and
760 Manley, 1992).
761
762 Linear corrections of -0.6 m ka^{-1} (subsidence) to 0.3 m ka^{-1} (uplift) provide an acceptable fit between
763 data and models in region 8, with a similar range of -0.7 m ka^{-1} (subsidence) to 0.8 m ka^{-1} (uplift) for
764 region 9 (Fig. 8). Notably, in region 9, index points for the last 1000 years are below present sea
765 level. This pattern, apparent from two sites separated by ~40 km, was previously recognised by
766 Garrett et al. (2015) and tentatively attributed to incomplete interseismic uplift following coseismic
767 subsidence during the 1960 earthquake. Interseismic uplift rates have been slowly increasing over
768 the past few decades (Melnick et al. 2018), a trend that would raise the dated sediments back
769 towards present sea level. In addition, effects at a local scale such as sediment compaction, or at a
770 larger scale such as neoglacial forebulge collapse, might influence RSL in this region over the last
771 millennium. While GIA model predictions generated using the ICE-6G ice model (Peltier et al., 2015)
772 in combination with relatively weak upper mantle viscosities replicate a late Holocene sea-level rise,
773 this signal may occur due to the low spatial resolution of the model and its inability to fully resolve

774 water loading and shoreline changes in this landscape of deep marine gulfs and mountains. The
775 cause of late Holocene sea-level rise in this region remains uncertain; nevertheless, its occurrence
776 provides accommodation space and may explain the preservation of palaeoseismic evidence at sites
777 in the region (Cisternas et al., 2005; 2017; Garrett et al., 2015).
778
779 Hervé and Ota (1993) inferred extremely fast tectonic uplift rates of 5 to 10 m ka^{-1} in regions 10 and
780 11 during the late Holocene. While we have rejected four of the seven dates in these regions due to
781 the possibility for reworking by extreme waves or human activity, the remaining three marine
782 limiting points require linear correction rates of > 14 m ka^{-1} (region 10) and > 5.5 m ka^{-1} (region 11)
783 to bring them in line with the model predictions (Fig. 8). While rapid uplift in region 10 may be
784 associated with the Liquiñe-Ofqui fault zone, further data are required to corroborate and extend
785 the record of RSL change in the continental region east of Isla de Chiloé.
786
787 6.3 Data paucity and areas for future focus
788
789 The Chilean sea-level database highlights the scarcity of sea-level data from northern Chile. Few
790 studies have focussed on the relative sea-level history in this region, or on allied endeavours that
791 may produce sea-level data points, such as coastal palaeoseismology. We attribute this lack to the
792 rarity of coastal fine-grained sedimentary depocentres and the terrestrial organic fossils to date
793 resulting from the region's aridity. To overcome this problem, future studies may consider rocky-
794 shore geomorphic markers and beach or beach ridge deposits that can be dated using marine shells
795 or through luminescence approaches. Such features have successfully provided sea-level data in
796 central Chile (Nelson and Manley, 1992; Bookhagen et al., 2006; Hart et al., 2017) and are present
797 along the coast of northern Chile. Future work should also focus on providing appropriate local
798 estimates of the indicative meaning of such features through surveying analogous modern sea-level
799 indicators and relating these to tidal datums.

While central and south-central Chile are more comprehensively represented in the database, the majority of sea-level data points are limited to the late Holocene and, particularly, the last 2 ka (Fig. 6). Consequently, there are few data to constrain key features of RSL history of this region. The height and timing of the mid-Holocene highstand remains a major uncertainty, with proxy reconstructions and GIA modelling indicating elevations between 2 and 6 m at Valdivia and between 0.5 and 7.5 m in the vicinity of the Chacao Channel.

7. Conclusions

The Chilean Holocene sea-level database presented in this paper provides a systematic, quality controlled, and internationally comparable database of sea-level data from the tectonically active coast of north, central and south-central Chile (18.5 – 43.6°S). We reinterpret indicative meanings (the relationship between a sea-level indicator and contemporaneous tidal levels), recalibrate ages, and fully assess all sources of error for sea-level indicators stemming from research into relative sea-level change, coastal palaeoseismology, palaeoclimatology, and archaeology. Much of the information on past sea levels provided by these sources has previously been overlooked. Our database summarises 166 accepted points, including 79 index points, 31 marine limiting points, and 56 terrestrial limiting points. We reject a further 53 data points due to ambiguities over the interpretation of depositional environments, the possibility of reworking by storm, fluvial, tsunami, or human activity, along with chronological inconsistencies.

The database includes sea-level data from four new sites presented here for the first time: Pelluhue (south of Constitución), Tubul (northern Arauco Peninsula), Punta Pájaros Niños (northern Isla Mocha), and Pilolcura (north of Valdivia). These sites illustrate how a range of different data sources, including alluvial deposits, marine shells, and intertidal sediments can provide constraints on past

826 sea level. Collectively, the new sites provide two marine limiting points, one terrestrial limiting point
827 and one index point.
828
829 Combining new and reassessed data, we use the database to describe relative sea-level histories for
830 11 coastal regions of Chile, noting the spatial inhomogeneity of the data. These histories highlight
831 substantial spatial differences in Holocene relative sea level: while the mid Holocene was
832 characterised by sea level above present in all regions, elevations vary from <5 m to 30 m.
833 Comparison of sea-level data with a suite of glacial isostatic adjustment models enables us to assess
834 the processes driving RSL change and highlights regions where millennial-scale tectonic deformation
835 may cause the data to significantly diverge from model predictions (particularly Isla Santa María, Isla
836 Mocha, and regions close to the Liquiñe-Ofqui fault zone). Uplift rates likely exceed 1 m ka^{-1} in these
837 regions and may be an order of magnitude greater over centennial timescales. We identify that no
838 net uplift is required to reconcile data and model predictions in many areas, including the southern
839 Bío Bío region, in contrast to the findings of an earlier study (Stefer et al., 2010).
840
841 We highlight northern Chile and the early to mid Holocene in all regions as particularly data poor.
842 Future efforts to address these data gaps will continue to assist efforts to address questions over the
843 driving mechanisms of sea-level variability (Khan et al., 2019). Furthermore, with the spatiotemporal
844 distribution of coastal archaeological and palaeoseismic evidence closely related to relative sea-level
845 change (Dickinson, 2011; Dura et al., 2016), the current Chilean sea-level database and future
846 advances in constraining RSL histories along the Chilean coast will support future research in these
847 and other fields.

Acknowledgements

EG undertook this work while in receipt of funding from the European Union/Durham University (COFUND under the DIFeREns 2 scheme). The authors acknowledge financial support from the Millennium Nucleus CYCLO "The Seismic Cycle Along Subduction Zones" funded by the Millennium Scientific Initiative (ICM) of the Chilean Government Grant Number NC160025. Additional support for MC and DM was provided by FONDECYT, project N° 1190258. TD was supported by National Science Foundation (NSF) awards EAR-1566253, EAR-1624795, and EAR-1624533. LE was supported by National Geographic Society Research Grant 8577-08 and NSF awards EAR-1036057, EAR-1145170, and EAR-1624542. JJM was supported by the Deutsche Forschungsgemeindschaft Grant JA 2860/1-1. The authors acknowledge PALSEA (a PAGES/INQUA working group) and HOLSEA (an INQUA project) for useful discussions at the 2019 meeting, Dublin, Ireland. We thank Nicole Khan and Matteo Vacchi for their constructive reviews. This is a contribution to International Geoscience Programme (IGCP) project 639. Any use of trade, firm, or product names is for descriptive purposes only and does not imply endorsement by the U.S. Government.

Data availability

The Chilean sea-level database is available via Mendeley Data:

http://dx.doi.org/10.17632/9459bd6gpt

References

Aniya, M., 1996. Holocene variations of Ameghino Glacier, southern Patagonia. The Holocene 6, 247–252.

Araneda, A., Torrejón, F., Aguayo, M., Torres, L., Cruces, F., Cisternas, M., Urrutia, R., 2007. Historical records of San Rafael glacier advances (North Patagonian Icefield): another clue to 'Little Ice Age' timing in southern Chile? The Holocene 17, 987–998.

874 Atwater, B.F., Núñez, H.J., Vita-Finzi, C., 1992. Net late Holocene emergence despite earthquake-
875 induced submergence, south-central Chile. Quaternary International 15, 77–85.
876 Barrientos, S., 2007. Earthquakes in Chile. The geology of Chile. The Geological Society, London 263–
877 287.
878 Bentley, M.J., McCulloch, R.D., 2005. Impact of neotectonics on the record of glacier and sea level
879 fluctuations, Strait of Magellan, southern Chile. Geografiska Annaler: Series A, Physical Geography
880 87, 393–402.
881 Bernard, F.R., 1983. Catalogue of the living bivalvia of the eastern Pacific Ocean: Bering Strait to
882 Cape Horn. Canadian Special Publication of Fisheries and Aquatic Sciences.
883 Bertrand, S., Hughen, K., Lamy, F., Stuut, J.B., Torejon, F., Lange, C., 2012. Precipitation as the main
884 driver of Neoglacial fluctuations of Gualas glacier, Northern Patagonian Icefield. Climate of the Past
885 8, 1–16.
886 Bloom, A.L., 1977. Atlas of Sea-level Curves: IGCP Project 61. International Geological Correlation
887 Program.
888 Bookhagen, B., Echtler, H.P., Melnick, D., Strecker, M.R., Spencer, J.Q.G., 2006. Using uplifted
889 Holocene beach berms for paleoseismic analysis on the Santa María Island, south-central Chile.
890 Geophysical Research Letters 33.
891 Brain, M.J., Long, A.J., Woodroffe, S.A., Petley, D.N., Milledge, D.G., Parnell, A.C., 2012. Modelling
892 the effects of sediment compaction on salt marsh reconstructions of recent sea-level rise. Earth
893 and Planetary Science Letters 345, 180–193.
894 Bronk Ramsey, C., 2009. Bayesian analysis of radiocarbon dates. Radiocarbon 51, 337–360.
895 Caldenius, C.C.Z., 1932. Las Glaciaciones Cuaternarias en la Patagonia y Tierra del Fuego: Una
896 investigación regional, estratigráfica y geocronológica.—Una comparación con la escala
897 geocronológica sueca. Geografiska Annaler 14, 1–164.
898 Cembrano, J., Hervé, F., Lavenu, A., 1996. The Liquiñe Ofqui fault zone: a long-lived intra-arc fault
899 system in southern Chile. Tectonophysics 259, 55–66.

900 Cisternas, M., Garrett, E., Wesson, R.L., Dura, T., Ely, L.L., 2017. Unusual geologic evidence of coeval
901 seismic shaking and tsunamis shows variability in earthquake size and recurrence in the area of the
902 giant 1960 Chile earthquake. Marine Geology 385, 101–113.
903 Cisternas, M., Atwater, B.F., Torrejón, F., Sawai, Y., Machuca, G., Lagos, M., Eipert, A., Youlton, C.,
904 Salgado, I., Kamataki, T., 2005. Predecessors of the giant 1960 Chile earthquake. Nature 437, 404–
905 407.
906 Creveling, J.R., Mitrovica, J.X., Hay, C.C., Austermann, J., Kopp, R.E., 2015. Revisiting tectonic
907 corrections applied to Pleistocene sea-level highstands. Quaternary Science Reviews 111, 72–80.
908 Dalton, A.S., Finkelstein, S.A., Forman, S.L., Barnett, P.J., Pico, T., Mitrovica, J.X., 2019. Was the
909 Laurentide ice sheet significantly reduced during marine isotope stage 3? Geology 47, 111–114.
910 Denton, G.H., Lowell, T. V, Heusser, C.J., Schlüchter, C., Andersen, B.G., Heusser, L.E., Moreno, P.I.,
911 Marchant, D.R., 1999. Geomorphology, stratigraphy, and radiocarbon chronology of Llanquihue
912 Drift in the area of the Southern Lake District, Seno Reloncaví, and Isla Grande de Chiloé, Chile.
913 Geografiska Annaler: Series A, Physical Geography 81, 167–229.
914 Dickinson, W.R., 2011. Geological perspectives on the Monte Verde archeological site in Chile and
915 pre-Clovis coastal migration in the Americas. Quaternary Research 76, 201–210.
916 Dura, T., Cisternas, M., Horton, B.P., Ely, L.L., Nelson, A.R., Wesson, R.L., Pilarczyk, J.E., 2015. Coastal
917 evidence for Holocene subduction-zone earthquakes and tsunamis in central Chile. Quaternary
918 Science Reviews 113, 93–111.
919 Dura, T., Engelhart, S.E., Vacchi, M., Horton, B.P., Kopp, R.E., Peltier, W.R., Bradley, S., 2016. The role
920 of Holocene relative sea-level change in preserving records of subduction zone earthquakes.
921 Current Climate Change Reports 2, 86–100.
922 Dura, T., Horton, B.P., Cisternas, M., Ely, L.L., Hong, I., Nelson, A.R., Wesson, R.L., Pilarczyk, J.E.,
923 Parnell, A.C., Nikitina, D., 2017. Subduction zone slip variability during the last millennium, south-
924 central Chile. Quaternary Science Reviews 175, 112–137.

925 Egbert, G.D., Erofeeva, S.Y., 2010. The OSU TOPEX/Poseidon Global Inverse Solution TPXO. Oregon
926 State University.
927 Ehlers, J., Gibbard, P.L., Hughes, P.D., 2011. Quaternary glaciations-extent and chronology: a closer
928 look. Elsevier.
929 Ely, L.L., Cisternas, M., Wesson, R.L., Dura, T., 2014. Five centuries of tsunamis and land-level
930 changes in the overlapping rupture area of the 1960 and 2010 Chilean earthquakes. Geology 42,
931 995–998. doi:10.1130/G35830.1
932 Encinas, A., Hervé, F., Villa-Martínez, R., Nielsen, S.N., Finger, K.L., Peterson, D.E., 2010. Finding of a
933 Holocene marine layer in Algarrobo (33 22'S), central Chile. Implications for coastal uplift. Andean
934 Geology 33, 339–345.
935 Engelhart, S.E., Vacchi, M., Horton, B.P., Nelson, A.R., Kopp, R.E., 2015. A sea-level database for the
936 Pacific coast of central North America. Quaternary Science Reviews 113, 78–92.
937 Farías, M., Vargas, G., Tassara, A., Carretier, S., Baize, S., Melnick, D., Bataille, K., 2010. Land-level
938 changes produced by the Mw 8.8 2010 Chilean earthquake. Science 329, 916.
939 Farrell, W.E., Clark, J.A., 1976. On Postglacial Sea Level. Geophysical Journal International 46, 647–
940 667.
941 Freed, A.M., Hashima, A., Becker, T.W., Okaya, D.A., Sato, H., Hatanaka, Y., 2017. Resolving depth-
942 dependent subduction zone viscosity and afterslip from postseismic displacements following the
943 2011 Tohoku-oki, Japan earthquake. Earth and Planetary Science Letters 459, 279–290.
944 Frugone-Álvarez, M., Latorre, C., Giralt, S., Polanco-Martínez, J., Bernárdez, P., Oliva-Urcia, B.,
945 Maldonado, A., Carrevedo, M.L., Moreno, A., Delgado Huertas, A., 2017. A 7000-year high-
946 resolution lake sediment record from coastal central Chile (Lago Vichuquén, 34° S): implications for
947 past sea level and environmental variability. Journal of Quaternary Science 32, 830–844.
948 García-Artola, A., Stéphan, P., Cearreta, A., Kopp, R.E., Khan, N.S., Horton, B.P., 2018. Holocene sea-
949 level database from the Atlantic coast of Europe. Quaternary Science Reviews 196, 177–192.

García, J.L., 2012. Late Pleistocene ice fluctuations and glacial geomorphology of the Archipiélago de Chiloé, southern Chile. Geografiska Annaler: Series A, Physical Geography 94, 459–479.

Garrett, E., Shennan, I., Woodroffe, S.A., Cisternas, M., Hocking, E.P., Gulliver, P., 2015. Reconstructing paleoseismic deformation, 2: 1000 years of great earthquakes at Chucalén, south central Chile. Quaternary Science Reviews 113, 112–122.

Garrett, E., Brader, M., Melnick, D., Bedford, J., Aedo, D., 2019. First Field Evidence of Coseismic Land-Level Change Associated with the 25 December 2016 Mw 7.6 Chiloé, Chile, Earthquake. Bulletin of the Seismological Society of America 109, 87–98.

Glasser, N.F., Harrison, S., Winchester, V., Aniya, M., 2004. Late Pleistocene and Holocene palaeoclimate and glacier fluctuations in Patagonia. Global and Planetary Change 43, 79–101.

Glasser, N.F., Jansson, K.N., Harrison, S., Kleman, J., 2008. The glacial geomorphology and Pleistocene history of South America between 38 S and 56 S. Quaternary Science Reviews 27, 365–390.

González-Acuña, J., Arroyo-Suarez, E., 2013. Comparative methodologies for sounding reduction applied to a bathymetric survey referred to the WGS-84 ellipsoid. Executed in Concepcion Bay and Gulf of Arauco, VIII Region, Chile., US Hydro 1.

Gordillo, S., Bujalesky, G.G., Pirazzoli, P.A., Rabassa, J.O., Saliège, J.-F., 1992. Holocene raised beaches along the northern coast of the Beagle Channel, Tierra del Fuego, Argentina. Palaeogeography, Palaeoclimatology, Palaeoecology 99, 41–54.

Hart, E.A., Stapor, F.W., Jerez, J.E.N., Sutherland, C.J., 2017. Progradation of a Beach Ridge Plain between 5000 and 4000 Years BP Inferred from Luminescence Dating, Coquimbo Bay, Chile. Journal of Coastal Research 33, 1065–1073.

Hervé, F., Ota, Y., 1993. Fast Holocene uplift rates at the Andes of Chiloé, southern Chile. Andean Geology 20, 15–23.

Heusser, C.J., Flint, R.F., 1977. Quaternary glaciations and environments of northern Isla Chiloé, Chile. Geology 5, 305–308.

976 Heusser, C.J., Streeter, S.S., 1980. A temperature and precipitation record of the past 16,000 years in
977 southern Chile. Science 210, 1345–1347.
978 Hijma, M.P., Engelhart, S.E., Törnqvist, T.E., Horton, B.P., Hu, P., Hill, D.F., 2015. A protocol for a
979 geological sea-level database. Handbook of Sea-Level Research, edited by: Shennan, I., Long, AJ,
980 and Horton, BP, Wiley Blackwell 536–553.
981 Hilleman, C., 2015. Upper-plate deformation following megathrust earthquakes: Holocene slip along
982 the El Yolki Fault in central Chile inferred from deformed coastal sediments. Masters Thesis,
983 University of Potsdam.
984 Hocking, E.P., Garrett, E., Cisternas, M., 2017. Modern diatom assemblages from Chilean tidal
985 marshes and their application for quantifying deformation during past great earthquakes. Journal
986 of Quaternary Science 32, 396–415.
987 Hogg, A.G., Hua, Q., Blackwell, P.G., Niu, M., Buck, C.E., Guilderson, T.P., Heaton, T.J., Palmer, J.G.,
988 Reimer, P.J., Reimer, R.W., 2013. SHCal13 Southern Hemisphere calibration, 0–50,000 years cal BP.
989 Radiocarbon 55, 1889–1903.
990 Hong, I., Dura, T., Ely, L.L., Horton, B.P., Nelson, A.R., Cisternas, M., Nikitina, D., Wesson, R.L., 2017. A
991 600-year-long stratigraphic record of tsunamis in south-central Chile. The Holocene 27, 39–51.
992 Horton, B.P., Shennan, I., 2009. Compaction of Holocene strata and the implications for relative
993 sealevel change on the east coast of England. Geology 37, 1083–1086.
994 Hua, Q., Barbetti, M., Rakowski, A.Z., 2013. Atmospheric radiocarbon for the period 1950–2010.
995 Radiocarbon 55, 2059–2072.
996 Hulton, N.R.J., Purves, R.S., McCulloch, R.D., Sugden, D.E., Bentley, M.J., 2002. The last glacial
997 maximum and deglaciation in southern South America. Quaternary Science Reviews 21, 233–241.
998 Ingram, B.L., Southon, J.R., 1996. Reservoir ages in eastern Pacific coastal and estuarine waters.
999 Radiocarbon 38, 573–582.

1000 Isla, F.I., Flory, J.Q., Martínez, C., Fernández, A., Jaque, E., 2012. The evolution of the Bío Bío delta
1001 and the coastal plains of the Arauco Gulf, Bío Bío Region: the Holocene sea-level curve of Chile.
1002 Journal of Coastal Research 28, 102–111.
1003 Isla, F.I., 1989. Holocene sea-level fluctuation in the southern hemisphere. Quaternary Science
1004 Reviews 8, 359–368.
1005 Jara-Muñoz, J., Melnick, D., 2015. Unravelling sea-level variations and tectonic uplift in wave-built
1006 marine terraces, Santa María Island, Chile. Quaternary Research 83, 216–228.
1007 Jara-Muñoz, J., Melnick, D., Brill, D., Strecker, M.R., 2015. Segmentation of the 2010 Maule Chile
1008 earthquake rupture from a joint analysis of uplifted marine terraces and seismic-cycle deformation
1009 patterns. Quaternary Science Reviews 113, 171–192.
1010 Jara-Muñoz, J., Melnick, D., Zambrano, P., Rietbrock, A., González, J., Argandoña, B., Strecker, M.R.,
1011 2017. Quantifying offshore fore-arc deformation and splay-fault slip using drowned Pleistocene
1012 shorelines, Arauco Bay, Chile. Journal of Geophysical Research: Solid Earth 122, 4529–4558.
1013 Kaizuka, S., Matsuda, T., Nogami, M., Yonekura, N., 1973. Quaternary tectonic and recent seismic
1014 crustal movements in the Arauco Peninsula and its environs, central Chile. Geographical Reports of
1015 Tokyo Metropolitan University 8, 1–49.
1016 Khan, N.S., Ashe, E., Horton, B.P., Dutton, A., Kopp, R.E., Brocard, G., Engelhart, S.E., Hill, D.F., Peltier,
1017 W.R., Vane, C.H., 2017. Drivers of Holocene sea-level change in the Caribbean. Quaternary Science
1018 Reviews 155, 13–36.
1019 Khan, N.S., Ashe, E., Shaw, T.A., Vacchi, M., Walker, J., Peltier, W.R., Kopp, R.E., Horton, B.P., 2015.
1020 Holocene relative sea-level changes from near-, intermediate-, and far-field locations. Current
1021 Climate Change Reports 1, 247–262.
1022 Khan, N.S., Horton, B.P., Engelhart, S., Rovere, A., Vacchi, M., Ashe, E.L., Törnqvist, T.E., Dutton, A.,
1023 Hijma, M.P., Shennan, I., 2019. Inception of a global atlas of sea levels since the Last Glacial
1024 Maximum. Quaternary Science Reviews 220, 359–371.

1025 Khazaradze, G., Wang, K., Klotz, J., Hu, Y., He, J., 2002. Prolonged post-seismic deformation of the
1026 1960 great Chile earthquake and implications for mantle rheology. Geophysical Research Letters
1027 29, 1–7.
1028 Klein, E., Vigny, C., Fleitout, L., Grandin, R., Jolivet, R., Rivera, E., Métois, M., 2017. A comprehensive
1029 analysis of the Illapel 2015 Mw8. 3 earthquake from GPS and InSAR data. Earth and Planetary
1030 Science Letters 469, 123–134.
1031 Lange, D., Cembrano, J., Rietbrock, A., Haberland, C., Dahm, T., Bataille, K., 2008. First seismic record
1032 for intra-arc strike-slip tectonics along the Liquiñe-Ofqui fault zone at the obliquely convergent
1033 plate margin of the southern Andes. Tectonophysics 455, 14–24.
1034 Lange, H., Casassa, G., Ivins, E.R., Schröder, L., Fritsche, M., Richter, A., Groh, A., Dietrich, R., 2014.
1035 Observed crustal uplift near the Southern Patagonian Icefield constrains improved viscoelastic
1036 Earth models. Geophysical Research Letters 41, 805–812.
1037 Leonard, E.M., Wehmiller, J.F., 1991. Geochronology of marine terraces at Caleta Michilla, northern
1038 Chile; implications for Late Pleistocene and Holocene uplift. Andean Geology 18, 81–86.
1039 Li, S., Bedford, J., Moreno, M., Barnhart, W.D., Rosenau, M., Oncken, O., 2018. Spatiotemporal
1040 variation of mantle viscosity and the presence of cratonic mantle inferred from 8 years of
1041 postseismic deformation following the 2010 Maule, Chile, earthquake. Geochemistry, Geophysics,
1042 Geosystems 19, 3272–3285.
1043 Lorenzo-Martín, F., Roth, F., Wang, R., 2006. Inversion for rheological parameters from post-seismic
1044 surface deformation associated with the 1960 Valdivia earthquake, Chile. Geophysical Journal
1045 International 164, 75–87.
1046 Marquardt, C., Lavenu, A., Ortlieb, L., Godoy, E., Comte, D., 2004. Coastal neotectonics in Southern
1047 Central Andes: uplift and deformation of marine terraces in Northern Chile (27 S). Tectonophysics
1048 394, 193–219.

May, S.M., Zander, A., Francois, J.P., Kelletat, D., Pötsch, S., Rixhon, G., Brückner, H., 2015. Chronological and geoarchaeological investigations on an anthropogenic shell accumulation layer in the Longotoma dune field (Central Chile). Quaternary International 367, 32–41.

May, S.M., Pint, A., Rixhon, G., Kelletat, D., Wennrich, V., Brückner, H., 2013. Holocene coastal stratigraphy, coastal changes and potential palaeoseismological implications inferred from geo-archives in Central Chile (29–32 S). Zeitschrift für Geomorphologie, Supplementary Issues 57, 201–228.

McCulloch, R.D., Bentley, M.J., Purves, R.S., Hulton, N.R.J., Sugden, D.E., Clapperton, C.M., 2000. Climatic inferences from glacial and palaeoecological evidence at the last glacial termination, southern South America. Journal of Quaternary Science: Published for the Quaternary Research Association 15, 409–417.

McCulloch, R.D., Davies, S.J., 2001. Late-glacial and Holocene palaeoenvironmental change in the central Strait of Magellan, southern Patagonia. Palaeogeography, Palaeoclimatology, Palaeoecology 173, 143–173.

Melnick, D., 2016. Rise of the central Andean coast by earthquakes straddling the Moho. Nature Geoscience 9, 401.

Melnick, D., Cisternas, M., Moreno, M., Norambuena, R., 2012. Estimating coseismic coastal uplift with an intertidal mussel: calibration for the 2010 Maule Chile earthquake (M w= 8.8). Quaternary Science Reviews 42, 29–42.

Melnick, D., Hillemann, C., Jara-Muñoz, J., Garrett, E., Cortés-Aranda, J., Molina, D., Tassara, A., Strecker, M.R., 2019. Hidden Holocene slip along the coastal El Yolki fault in Central Chile and its possible link with megathrust earthquakes. Journal of Geophysical Research: Solid Earth *124*. https://doi.org/10.1029/ 2018JB017188.

Melnick, D., Li, S., Moreno, M., Cisternas, M., Jara-Muñoz, J., Wesson, R., Nelson, A., Báez, J.C., Deng, Z., 2018. Back to full interseismic plate locking decades after the giant 1960 Chile earthquake. Nature communications 9, 3527.

1075 Mercer, J.H., 1970. Variations of some Patagonian glaciers since the Late-Glacial; II. American Journal
1076 of Science 269, 1–25.
1077 Nelson, A.R., Kashima, K., Bradley, L.-A., 2009. Fragmentary evidence of great-earthquake
1078 subsidence during Holocene emergence, Valdivia Estuary, south central Chile. Bulletin of the
1079 Seismological Society of America 99, 71–86.
1080 Nelson, A.R., Manley, W.F., 1992. Holocene coseismic and aseismic uplift of Isla Mocha, south-
1081 central Chile. Quaternary International 15, 61–76.
1082 Orford, J.D., Carter, R.W.G., Jennings, S.C., 1991. Coarse clastic barrier environments: evolution and
1083 implications for Quaternary sea level interpretation. Quaternary International 9, 87–104.
1084 Ortlieb, L., Vargas, G., Saliège, J.-F., 2011. Marine radiocarbon reservoir effect along the northern
1085 Chile–southern Peru coast (14–24 S) throughout the Holocene. Quaternary Research 75, 91–103.
1086 Ota, Y., Paskoff, R., 1993. Holocene deposits on the coast of north-central Chile: radiocarbon ages
1087 and implications for coastal changes. Andean Geology 20, 25–32.
1088 Otvos, E.G., 2000. Beach ridges—definitions and significance. Geomorphology 32, 83–108.
1089 Peltier, W.R., 2004. Global glacial isostasy and the surface of the ice-age Earth: the ICE-5G (VM2)
1090 model and GRACE. Annual Reviews of Earth and Planetary Science 32, 111–149.
1091 Peltier, W.R., Argus, D.F., Drummond, R., 2015. Space geodesy constrains ice age terminal
1092 deglaciation: The global ICE-6G_C (VM5a) model. Journal of Geophysical Research: Solid Earth 120,
1093 450–487.
1094 Pico, T., Creveling, J.R., Mitrovica, J.X., 2017. Sea-level records from the US mid-Atlantic constrain
1095 Laurentide Ice Sheet extent during Marine Isotope Stage 3. Nature Communications 8, 1–6.
1096 Pino, M., Navarro, R.X., 2005. Geoarqueología del sitio arcaico Chan-Chan 18, costa de Valdivia:
1097 discriminación de ambientes de ocupación humana y su relación con la transgresión marina del
1098 Holoceno Medio. Revista geológica de Chile 32, 59–75.
1099 Pirazzoli, P.A., 1991. World atlas of Holocene sea-level changes. Elsevier.

1100 Plafker, G., Savage, J.C., 1970. Mechanism of the Chilean earthquakes of May 21 and 22, 1960.
1101 Geological Society of America Bulletin 81, 1001–1030.
1102 Porter, S.C., Stuiver, M., Heusser, C.J., 1984. Holocene sea-level changes along the Strait of Magellan
1103 and Beagle Channel, southernmost South America. Quaternary Research 22, 59–67.
1104 Rabassa, J., Clapperton, C.M., 1990. Quaternary glaciations of the southern Andes. Quaternary
1105 Science Reviews 9, 153–174.
1106 Rabassa, J., Heusser, C., Stuckenrath, R., 1986. New data on Holocene sea transgression in the
1107 Beagle Channel: Tierra del Fuego, Argentina, in: International Symposium on Sea-Level Changes
1108 and Quaternary Shorelines. pp. 291–309.
1109 Rehak, K., Strecker, M.R., Echtler, H.P., 2008. Morphotectonic segmentation of an active forearc, 37–
1110 41 S, Chile. Geomorphology 94, 98–116.
1111 Reimer, P.J., Bard, E., Bayliss, A., Beck, J.W., Blackwell, P.G., Bronk Ramsey, C., Buck, C.E., Cheng, H.,
1112 Edwards, R.L., Friedrich, M., 2013. IntCal13 and Marine13 radiocarbon age calibration curves 0-
1113 50,000 years cal BP. Radiocarbon 55, 1869–1887.
1114 Reyes, O., Méndez, C., San Román, M., Francois, J.-P., 2018. Earthquakes and coastal archaeology:
1115 Assessing shoreline shifts on the southernmost Pacific coast (Chonos Archipelago 43 50'–46 50' S,
1116 Chile, South America). Quaternary International 463, 161–175.
1117 Richter, A., Ivins, E., Lange, H., Mendoza, L., Schröder, L., Hormaechea, J.L., Casassa, G., Marderwald,
1118 E., Fritsche, M., Perdomo, R., 2016. Crustal deformation across the Southern Patagonian Icefield
1119 observed by GNSS. Earth and Planetary Science Letters 452, 206–215.
1120 Rignot, E., Rivera, A., Casassa, G., 2003. Contribution of the Patagonia Icefields of South America to
1121 sea level rise. Science 302, 434–437.
1122 Rosenau, M., Melnick, D., Echtler, H., 2006. Kinematic constraints on intra-arc shear and strain
1123 partitioning in the southern Andes between 38 S and 42 S latitude. Tectonics 25.

1124 Schellmann, G., Radtke, U., 2010. Timing and magnitude of Holocene sea-level changes along the
1125 middle and south Patagonian Atlantic coast derived from beach ridge systems, littoral terraces and
1126 valley-mouth terraces. Earth-Science Reviews 103, 1–30.
1127 Shennan, I., 2015. Framing research questions, in: Shennan, I., Long, A.J., Horton, B.P. (Eds.),
1128 Handbook of Sea-Level Research. John Wiley & Sons, pp. 3–25.
1129 Shennan, I., Bradley, S.L., Edwards, R., 2018. Relative sea-level changes and crustal movements in
1130 Britain and Ireland since the Last Glacial Maximum. Quaternary Science Reviews 188, 143–159.
1131 Shennan, I., Milne, G., Bradley, S., 2012. Late Holocene vertical land motion and relative sea-level
1132 changes: lessons from the British Isles. Journal of Quaternary Science 27, 64–70.
1133 Shennan, I., Peltier, W.R., Drummond, R., Horton, B., 2002. Global to local scale parameters
1134 determining relative sea-level changes and the post-glacial isostatic adjustment of Great Britain.
1135 Quaternary Science Reviews 21, 397–408.
1136 Stefer, S., Moernaut, J., Melnick, D., Echtler, H.P., Arz, H.W., Lamy, F., De Batist, M., Oncken, O.,
1137 Haug, G.H., 2010. Forearc uplift rates deduced from sediment cores of two coastal lakes in south-
1138 central Chile. Tectonophysics 495, 129–143.
1139 Tamura, T., 2012. Beach ridges and prograded beach deposits as palaeoenvironment records. Earth-
1140 Science Reviews 114, 279–297.
1141 Taylor, R.E., Berger, R., 1967. Radiocarbon content of marine shells from the Pacific coasts of Central
1142 and South America. Science 158, 1180–1182.
1143 Vacchi, M., Marriner, N., Morhange, C., Spada, G., Fontana, A., Rovere, A., 2016. Multiproxy
1144 assessment of Holocene relative sea-level changes in the western Mediterranean: sea-level
1145 variability and improvements in the definition of the isostatic signal. Earth-Science Reviews 155,
1146 172–197.
1147 Vacchi, M., Engelhart, S.E., Nikitina, D., Ashe, E.L., Peltier, W.R., Roy, K., Kopp, R.E., Horton, B.P.,
1148 2018. Postglacial relative sea-level histories along the eastern Canadian coastline. Quaternary
1149 Science Reviews 201, 124–146.

Van de Plassche, O., 1986. Sea-level research: A manual for the collection and evaluation of data: Norwich. UK, Geobooks.

Villa-Martínez, R., Villagrán, C., 1997. Historia de la vegetación de bosques pantanosos de la costa de Chile central durante el Holoceno medio y tardío. Revista Chilena de Historia Natural 70, 391–401.

Villalobos Silva, M.P., 2005. Evidencias de la fluctuación del nivel del mar y alzamientos tectónicos desde el Pleistoceno tardío en isla Mancera X Región de Los Lagos-Chile: registro estratigráfico y sedimentológico. Doctoral Thesis, Universidad Austral de Chile.

Von Huene, R., Kulm, L.D., Miller, J., 1985. Structure of the frontal part of the Andean convergent margin. Journal of Geophysical Research: Solid Earth 90, 5429–5442.

Wesson, R.L., Cisternas, M., Ely, L.L., Melnick, D., Briggs, R.W., Garrett, E., 2014. Uncertainties in field estimation of mean sea level, in: Barlow, N.L.M., Koehler, R. (Eds.), Seismic and Non-Seismic Influences on Coastal Change in Alaska. Alaska Division of Geological and Geophysical Surveys Guidebook, p. 165pp.

Willis, M.J., Melkonian, A.K., Pritchard, M.E., Rivera, A., 2012. Ice loss from the Southern Patagonian ice field, South America, between 2000 and 2012. Geophysical Research Letters 39, L17501.

Wiseman, K., Bürgmann, R., Freed, A.M., Banerjee, P., 2015. Viscoelastic relaxation in a heterogeneous Earth following the 2004 Sumatra–Andaman earthquake. Earth and Planetary Science Letters 431, 308–317.

Xu, W., 2017. Finite-fault Slip Model of the 2016 Mw 7.5 Chiloé Earthquake, Southern Chile, Estimated from Sentinel-1 Data. Geophysical Research Letters 44, 4774–4780.